

Interstellar Extinction and Elemental Abundances: Individual Sight Lines

DRAFT: 2021.11.9.200

Wenbo Zuo^{1,2,3}, Aigen Li³ and Gang Zhao^{1,2,3}

ABSTRACT

While it is well recognized that both the Galactic interstellar extinction curves and the gas-phase abundances of dust-forming elements exhibit considerable variations from one sightline to another, as yet most of the dust extinction modeling efforts have been directed to the Galactic average extinction curve, which is obtained by averaging over many clouds of different gas and dust properties. Therefore, any details concerning the relationship between the dust properties and the interstellar environments are lost. Here we utilize the wealth of extinction and elemental abundance data obtained by space telescopes and explore the dust properties of a large number of individual sightlines. We model the observed extinction curve of each sightline and derive the abundances of the major dust-forming elements (i.e., C, O, Si, Mg and Fe) required to be tied up in dust (i.e., dust depletion). We then confront the derived dust depletions with the observed gas-phase abundances of these elements and investigate the environmental effects on the dust properties and elemental depletions. It is found that for the majority of the sightlines the interstellar oxygen atoms are fully accommodated by gas and dust and therefore there does not appear to be a “missing oxygen” problem. For those sightlines with an extinction-to-hydrogen column density $A_V/N_H \gtrsim 4.8 \times 10^{-22} \text{ mag cm}^2 \text{ H}^{-1}$ there are shortages of C, Si, Mg and Fe elements for making dust to account for the observed extinction, even if the interstellar C/H, Si/H, Mg/H and Fe/H abundances are assumed to be protosolar abundances augmented by Galactic chemical evolution.

¹CAS Key Laboratory of Optical Astronomy, National Astronomical Observatories, Chinese Academy of Sciences, Beijing 100101, China; gzhao@nao.cas.cn

²School of Astronomy and Space Science, University of Chinese Academy of Sciences, Beijing 100049, China

³Department of Physics and Astronomy, University of Missouri, Columbia, MO 65211, USA; lia@missouri.edu

Subject headings: Gas-to-dust ratio (638); Interstellar dust extinction (837); Interstellar dust (836); Cosmic abundances (315); Interstellar abundances (832); Solar abundances (1474)

1. Introduction

The interstellar extinction and abundances of metal elements provide important clues about the size distribution and chemical makeup of interstellar dust. While it has been well recognized that the interstellar extinction curves exhibit considerable variations from one sight line to another (e.g., see Witt et al. 1984, Siebenmorgen et al. 2018), most of the extinction modeling efforts have been so far directed to the *mean* extinction curve of the Galaxy, obtained by averaging over many clouds of different gas and dust properties (e.g., see Mathis et al. 1977, Draine & Lee 1984, Désert et al. 1990, Siebenmorgen & Krügel 1992, Mathis 1996, Li & Greenberg 1997, Li & Draine 2001a, Weingartner & Draine 2001, Zubko et al. 2004, Jones et al. 2013). Cardelli et al. (1989) found that the Galactic average extinction curve can be approximated by an analytical formula (known as the CCM formula or parameterization) characterized by $R_V \approx 3.1$, where $R_V \equiv A_V/E(B - V)$ is the optical total-to-selective extinction ratio and $E(B - V) \equiv A_B - A_V$ is the reddening or color excess between the visual extinction A_V and the B -band extinction A_B .

Depending on the local physical conditions, the CCM parameterization of the extinction curves of various individual sight lines involves a wide range of R_V values which deviate substantially from the Galactic average value of $R_V \approx 3.1$ (e.g., see Fitzpatrick et al. 2019). More specifically, low-density regions usually have a smaller R_V for which the extinction curve is characterized by a strong 2175 Å bump and a steep far ultraviolet (UV) rise at $\lambda^{-1} > 6 \mu\text{m}^{-1}$. In contrast, sight lines penetrating into dense clouds, such as the Ophiuchus or Taurus molecular clouds, usually have $4 < R_V < 6$ and their extinction curves exhibit a weak 2175 Å bump and a relatively flat far-UV rise. Also, the extinction curves toward some sight lines are “anomalous”, i.e., they deviate considerably from that expected from the R_V -based CCM parameterization (e.g., see Cardelli & Clayton 1991, Mazzei & Barbaro 2011). Apparently, the dust size and composition properties of those “anomalous” sight lines or those with R_V values appreciably smaller or larger the canonical $R_V = 3.1$ are naturally expected to differ from that deduced from the Galactic average extinction curve. Therefore, by modeling the Galactic average extinction curve, unavoidably, any details concerning the relationship between the dust properties and the physical and chemical conditions of the interstellar environments would have been lost.

Interstellar dust is made of metal elements produced in stars, especially carbon (C), oxygen (O), silicon (Si), magnesium (Mg) and iron (Fe). Space-borne UV spectroscopic observations of interstellar clouds have provided important data on the abundances of components of interstellar gas and have revealed that the gas-phase abundances of heavy elements are significantly lower, relative to hydrogen (H), than in the solar photosphere. As those elements “missing” from the gas phase must have condensed into dust grains, the striking abundance deficiencies of heavy elements such as Si, Mg, Fe, and to a lesser degree, C and O—known as “interstellar depletion”—provide useful information on the possible composition and mass (relative to gas) of interstellar dust (e.g., see Kimura et al. 2003a,b, Voshchinnikov & Henning 2010). Apparently, any viable interstellar dust model should not contradict the interstellar depletion.

To quantitatively assess the constraints on the composition and quantity of interstellar dust placed by interstellar depletion, one has to assume a nominal reference abundance standard which describes the total abundance of an element in the combined gas-plus-dust phases. The dust-phase abundance of an element is then determined by subtracting off the gas-phase abundance from the assumed reference abundance. Apparently, the abundance constraints on interstellar dust sensitively rely on the knowledge of the gas-phase abundances of dust-forming elements and the assumption of the reference abundance (also known as “interstellar abundance”, or “cosmic abundance”).

However, what might be the most appropriate set of interstellar reference abundances remains unclear. The interstellar abundances are often assumed to be solar (e.g., see Whittet 1984), subsolar (like that of B stars and young F and G stars; see Snow & Witt 1995, 1996, Sofia & Meyer 2001), and protosolar (see Lodders 2003).¹ More recently, it has been argued that the interstellar abundances are better represented by the protosolar abundances augmented by Galactic chemical enrichment (GCE; see Zuo et al. 2021, Hensley & Draine 2021). Nevertheless, a very recent observational study carried out by De Cia et al. (2021) implied that the interstellar abundances of refractory elements in the local Galactic interstellar medium (ISM) may only be about 55% solar on average, though with a high degree of variation. This would place stringent constraints on dust models.

Also, the overall Galactic average interstellar gas abundances for the dust-forming elements remain uncertain. Most dust extinction modeling efforts assume that the gas-phase abundances of C and O are invariable with respect to the local interstellar conditions (e.g.,

¹The protosolar abundance of an element (except H) is the present-day solar photospheric abundance of that element *increased* by correcting for the settling effects. The currently observed solar photospheric abundances (relative to H) must be lower than those of the proto-Sun because helium and other heavy elements have settled toward the solar interior since the time of its formation ~ 4.55 Gyr ago (Lodders 2003).

see Cardelli et al. 1996, Meyer et al. 1998) and that Si, Mg and Fe are fully depleted from the gas. However, numerous observational studies carried out in the past decade have shown that the gas-phase C/H and O/H abundances vary with the local conditions (see Zuo et al. 2021 and references therein) and that in many sightlines there are nontrivial amounts of gas-phase Si, Mg and Fe (e.g., see Jensen et al. 2010). Therefore, in modeling the Galactic average extinction curve, the assumption of constant gas-phase abundances for the dust-forming elements would also unavoidably cause the loss of all the details concerning the abundance constraints on the dust properties and particularly their relation to the physical and chemical conditions of the interstellar environments.

In view of the shortcomings of modeling the Galactic *average* extinction curve and assuming a set of *constant, environmentally-invariable* gas-phase abundances for the dust-forming elements, in this work we are motivated to model the extinction curves of individual sight lines from the far-UV to the near infrared (IR), with the aid of abundance constraints. To this end, we confine ourselves to those sight lines for which the gas-phase abundances of one or more of the dust-forming elements have been observationally determined. This stands in contrast to the common practice of modeling the Galactic *average* extinction curve under the assumption of *constant* gas-phase abundances. This paper is organized as follows. We first compile in §2 a complete sample of all the (81) Galactic sightlines for which the extinction curves from the far-UV to the near-IR as well as the gas-phase abundances of at least one of the dust-forming elements (i.e., C, O, Mg, Si, and Fe) have been observationally measured. We then model in §3 the extinction curves of 45 individual sight lines in terms of the standard silicate-graphite interstellar grain model since previously 36 sight lines have already been modeled by one of us (Mishra & Li 2015, 2017). The results are discussed in §4 and summarized in §5.

2. Extinction Curves of Individual Sight Lines

We first search for in the literature an as complete as possible set of individual interstellar sight lines for which both the extinction curves have been observationally determined from the near-IR to the far-UV and the gas-phase abundances have been measured for at least one of the dust-forming elements (i.e., C, O, Mg, Si, and Fe). As a result, we find 81 such sight lines and tabulate in Table 1 the extinction parameters $c'_1, c'_2, c'_3, c'_4, x_0$ and γ as well as $E(B - V)$, R_V and $A_U, A_B, A_V, A_J, A_H, A_K$, the extinction at the U, B, V, J, H, K bands, respectively. We tabulate in Table 2 the gas-phase abundances of C, O, Mg, Si, and Fe as well as the column densities of atomic hydrogen $N(\text{HI})$, molecular hydrogen $N(\text{H}_2)$, the total hydrogen column densities $N_{\text{H}} = N(\text{HI}) + 2N(\text{H}_2)$, and the fraction of H in molecular form

$f(\text{H}_2)$.

For each sight line, we construct the extinction curve as follows.² First, we make use of the extinction parameters $c'_1, c'_2, c'_3, c'_4, x_o, \gamma$ and A_V tabulated in Table 1 to represent the UV extinction measured by the *International Ultraviolet Explorer* (IUE) at $3.3 < \lambda^{-1} < 8.7 \mu\text{m}^{-1}$ as a sum of three components: a linear background, a Drude profile for the 2175 Å extinction bump, and a far-UV nonlinear rise at $\lambda^{-1} > 5.9 \mu\text{m}^{-1}$:

$$A_\lambda = A_V \times \{c'_1 + c'_2 x + c'_3 D(x, \gamma, x_o) + c'_4 F(x)\} \quad , \quad (1)$$

$$D(x, \gamma, x_o) = \frac{x^2}{(x^2 - x_o^2)^2 + x^2 \gamma^2} \quad , \quad (2)$$

$$F(x) = \begin{cases} 0 , & x < 5.9 \mu\text{m}^{-1} \quad , \\ 0.5392 (x - 5.9)^2 + 0.05644 (x - 5.9)^3 , & x \geq 5.9 \mu\text{m}^{-1} \quad , \end{cases} \quad (3)$$

where A_λ is the extinction at wavelength λ , $x \equiv 1/\lambda$ is the inverse wavelength in μm^{-1} , c'_1 and c'_2 define the linear background, c'_3 defines the strength of the 2175 Å extinction bump which is approximated by $D(x, \gamma, x_o)$, a Drude function which peaks at $x_o \approx 4.6 \mu\text{m}^{-1}$ and has a full-width-half-maximum (FWHM) of γ , and c'_4 defines the nonlinear far-UV rise. This parameterization was originally introduced by Fitzpatrick & Massa (1990; hereafter FM90) for the interstellar reddening

$$E(\lambda - V)/E(B - V) = R_V (A_\lambda/A_V - 1) = c_1 + c_2 x + c_3 D(x, \gamma, x_o) + c_4 F(x) \quad , \quad (4)$$

where $E(\lambda - V) \equiv A_\lambda - A_V$. The extinction parameters c'_j listed here in Table 1 (taken from Valencic et al. 2004) relate to the FM90 parameters through

$$c'_j = \begin{cases} c_j/R_V + 1 , & j = 1 \quad , \\ c_j/R_V , & j = 2, 3, 4 \quad . \end{cases} \quad (5)$$

In the following, we will refer to the parameterization described by Equations (1–3) as the FM parameterization.

For $1.1 < \lambda^{-1} < 3.3 \mu\text{m}^{-1}$, we compute the extinction A_λ from the CCM parameterization which involves only one parameter (i.e., R_V). As illustrated in Figure 1a of Zuo et al.

²We have previously already taken the same approach to construct the extinction curves for a “gold” sample of 10 sight lines for which the gas-phase abundances of *all* the five major dust-forming elements C, O, Mg, Si and Fe have been observationally measured (see Zuo et al. 2021). Therefore, we are left with 71 sight lines for extinction-curve construction.

(2021), there is often a discontinuity between the FM parameterization at $\lambda^{-1} > 3.3 \mu\text{m}^{-1}$ and the CCM parameterization at $\lambda^{-1} < 3.3 \mu\text{m}^{-1}$. To comply with the observed extinction-to-gas ratio A_V/N_H , we multiply the FM extinction curve by a factor to smoothly join the CCM curve (see Figure 1b of Zuo et al. 2021).

For $0.9 \mu\text{m} < \lambda < 1 \text{ cm}$, we approximate the extinction either by the model extinction calculated from the standard silicate-graphite-PAH model of Weingartner & Draine (2001; WD01) for $R_V = 3.1$, or by the model extinction calculated by Wang, Li, & Jiang (2015a; WLJ15). The WLJ15 model is essentially the same as WD01 but includes an extra population of very large, micron-sized graphitic grains which was invoked to account for the observed flat mid-IR extinction at $3 < \lambda < 8 \mu\text{m}$. Therefore, for each of the 71 sight lines we construct two extinction curves (which we refer to as “WD01” and “WLJ15”).

The synthesized extinction curves for the 71 sight lines are shown in Figures 1–12. Whenever available, the broadband photometric extinction data at the U, B, V, J, H and K bands are superimposed as black squares on the extinction curves. It is apparent that the synthesized extinction curves of all 49 sightlines for which the U, B, and V extinction data are available closely agree with the observationally-determined U, B and V extinction. It is also clear that, for the majorities (24/29) of the sight lines for which the J, H and K extinction data are available, the WLJ15 curves closely agree the observationally-determined J, H and K extinction, suggesting that the WLJ15 model may be a realistic representation of the near- and mid-IR extinction. While the WD01 curve approximately agrees with the J, H, and K extinction data of HD 25443 (see Figure 2), it appreciably exceeds the J and H extinction data of HD 197512 (see Figure 10) and HD 220057 (see Figure 12). On the other hand, the WLJ15 curves of HD 38087 (see Figure 2) and HD 179789 (see Figure 9) are somewhat lower than their J, H and K extinction data.

3. Interstellar Extinction Modeling

We now model the extinction curve of each sight line to derive the dust size distributions and the abundances of C, O, Si, Mg and Fe required to be depleted in dust. We consider the standard silicate-graphite interstellar grain model which consists of two separate dust components: amorphous silicate and graphite (Mathis et al. 1977, Draine & Lee 1984). For simplicity, we assume the dust to be spherical in shape. We adopt an exponentially-cutoff power-law size distribution for both components: $dn_i/da = n_H B_i a^{-\alpha_i} \exp(-a/a_{c,i})$ for the size range of $50 \text{ \AA} < a < 2.5 \mu\text{m}$, where a is the spherical radius of the dust, n_H is the number density of H nuclei, dn_i is the number density of dust of type i with radii in the interval $[a, a + da]$, α_i and $a_{c,i}$ are respectively the power index and exponential cutoff size for dust

of type i , and B_i is the constant related to the total amount of dust of type i . The total extinction per H column at wavelength λ is given by

$$A_\lambda/N_{\text{H}} = 1.086 \sum_i \int da \frac{1}{n_{\text{H}}} \frac{dn_i}{da} C_{\text{ext},i}(a, \lambda), \quad (6)$$

where the summation is over the two grain types (i.e., silicate and graphite), and $C_{\text{ext},i}(a, \lambda)$ is the extinction cross section of grain type i of size a at wavelength λ which can be calculated from Mie theory (Bohren & Huffman 1983) using the dielectric functions of “astronomical” silicate and graphite of Draine & Lee (1984).

The upper cutoff size of $a_{\text{max}} = 2.5 \mu\text{m}$ is chosen because the amount of large grains of $a > 2.5 \mu\text{m}$ is negligible. As a matter of fact, we will see later that for most of the sight lines, the exponential cutoff sizes ($a_{c,S} \lesssim 0.2 \mu\text{m}$ for silicate, $a_{c,C} \lesssim 0.5 \mu\text{m}$ for graphite; see Table 3) are all much smaller than $a_{\text{max}} = 2.5 \mu\text{m}$. This justifies that the choice of $a_{\text{max}} = 2.5 \mu\text{m}$. On the other hand, the presence in the ISM of a population of angstrom- and nano-sized grains is revealed by the emission detected by the *Infrared Astronomical Satellite* (IRAS) broadband photometry at 12 and 25 μm and later confirmed by the *Diffuse Infrared Background Experiment* (DIRBE) instrument on the *Cosmic Background Explorer* (COBE) satellite (see Li 2004 and references therein), as well as by the so-called “unidentified infrared emission (UIE)” bands at 3.3, 6.2, 7.7, 8.6, 11.3 and 12.7 μm which are commonly attributed to polycyclic aromatic hydrocarbon (PAH) molecules (Allamandola et al. 1985, Léger & Puget 1984, Li 2020). The lower cutoff size of $a_{\text{min}} = 50 \text{ \AA}$ is chosen because angstrom- and nano-sized grains are in the Rayleigh regime (i.e., $2\pi a/\lambda \ll 1$) in the far-UV and, on a per unit volume basis, their extinction cross sections are independent of grain size a and, therefore, the observed far-UV extinction is not able to constrain the size distribution of angstrom- and nano-sized grains. Instead, it is the near- and mid-IR emission that allows one to derive the size distribution of grains of $a < 50 \text{ \AA}$ (see Li & Draine 2001a).

In fitting the extinction curve, for a given sightline, we have six parameters: the size distribution power indices α_S and α_C for silicate and graphite, respectively; the exponential cutoff sizes $a_{c,S}$ and $a_{c,C}$ for silicate and graphite, respectively; and B_S and B_C . We derive the silicon and carbon depletions from

$$[\text{Si}/\text{H}]_{\text{dust}} = (n_{\text{H}} B_S / 172 m_{\text{H}}) \int da (4\pi/3) a^3 \rho_{\text{sil}} a^{-\alpha_S} \exp(-a/a_{c,S}) \quad , \quad (7)$$

$$[\text{C}/\text{H}]_{\text{dust}} = (n_{\text{H}} B_C / 12 m_{\text{H}}) \int da (4\pi/3) a^3 \rho_{\text{gra}} a^{-\alpha_C} \exp(-a/a_{c,C}) \quad , \quad (8)$$

where we assume a stoichiometric composition of MgFeSiO_4 for amorphous silicate (of which the molecular weight is $\mu_{\text{sil}} \approx 172 m_{\text{H}}$) so that the abundances of O, Mg and Fe tied up in

dust are respectively $[\text{O}/\text{H}]_{\text{dust}} \approx 4 \times [\text{Si}/\text{H}]_{\text{dust}}$, $[\text{Mg}/\text{H}]_{\text{dust}} \approx [\text{Si}/\text{H}]_{\text{dust}}$, and $[\text{Fe}/\text{H}]_{\text{dust}} \approx [\text{Si}/\text{H}]_{\text{dust}}$. As mentioned earlier, both silicate and graphitic grains are taken to be larger than $a_{\text{min}} = 50 \text{ \AA}$ and thus nano silicate grains are not considered here, although an appreciable amount of nano silicate grains may be present in the ISM (Li & Draine 2001b, Hoang et al. 2016, Hensley & Draine 2017). Also, PAHs are not included in the extinction modeling and the 2175 Å extinction bump is attributed to small graphitic grains.

For a given sightline, we seek the best fit to the extinction between $0.3 \mu\text{m}^{-1}$ and $8 \mu\text{m}^{-1}$ by varying the size distribution power indices α_{S} and α_{C} , and the upper cutoff size parameters $a_{\text{c,S}}$ and $a_{\text{c,C}}$. Following WD01, we evaluate the extinction at 100 wavelengths λ_i , equally spaced in $\ln \lambda$. We use the Levenberg-Marquardt method (Press et al. 1992) to minimize χ^2 which gives the error in the extinction fit:

$$\chi^2 = \sum_i \frac{(\ln A_{\text{obs}} - \ln A_{\text{mod}})^2}{\sigma_i^2}, \quad (9)$$

where $A_{\text{obs}}(\lambda_i)$ is the observed extinction at wavelength λ_i , $A_{\text{mod}}(\lambda_i)$ is the extinction computed for the model at wavelength λ_i (see eq. 6), and the σ_i are weights. Following WD01, we take the weights $\sigma_i^{-1} = 1$ for $1.1 < \lambda^{-1} < 8 \mu\text{m}^{-1}$ and $\sigma_i^{-1} = 1/3$ for $\lambda^{-1} < 1.1 \mu\text{m}^{-1}$.

Among the 81 sight lines compiled in this work, Mishra & Li (2015, 2017) have already modeled the extinction curves for 36 sightlines in the same manner as described above. In this work, we model the remaining 45 sight lines and the best-fit model parameters are tabulated in Table 3. As shown in Figures 13–20, a simple mixture of silicate and graphite is capable of closely reproducing the observed extinction curves of almost all sight lines from the UV to the near-IR. The only exception is HD 93222 for which the model produces too broad a 2175 Å extinction bump to be comparable to the observed bump (see Figure 16). Indeed, HD 93222 is rather unusual in the sense that, while its extinction curve at $\lambda^{-1} < 4 \mu\text{m}^{-1}$ is characteristic of dense regions as reflected by its large $R_V = 4.76$, it exhibits a sharp 2175 Å bump and a steep far-UV rise at $\lambda^{-1} > 5.9 \mu\text{m}^{-1}$ which are both characteristic of a small R_V for diffuse regions (i.e., $R_V < 3.1$). A more thorough exploration of HD 93222 will be presented in a separate paper.

It is gratifying that the simple silicate-graphite model also successfully fits the “anomalous” extinction curves of HD 62542 (see Figure 15) and HD 210121 (see Figure 20). The line of sight toward the B5V star HD 62542 passes through a dense cloud in the Gum nebula region. Its extinction curve shows an exceedingly anomalous 2175 Å extinction bump of which the central wavelength shifts from the canonical 2175 Å to 2110 Å, and its width ($\sim 1.3 \mu\text{m}^{-1}$) is substantially broader than the Galactic average of $\sim 0.99 \mu\text{m}^{-1}$ (Cardelli & Savage 1988). The high-latitude cirrus cloud toward the B3V star HD 210121 also exhibits an anomalous extinction curve which deviates considerably from the CCM parameterization

expected from its small $R_V \approx 2.1$ (Larson et al. 1996). Its extinction curve is characterized by an extremely steep far-UV rise and by a weak and broad 2200 Å hump (Welty & Fowler 1992, Li & Greenberg 1998). The robustness of the silicate-graphite model in modeling the extinction curves of individual sight lines is demonstrated in Figures 13–20 where a wide range of extinction-curve shapes are accounted for, including the extremely anomalous extinction curves seen in the lines of sight toward HD 62542 and HD 210121.

4. Discussion

As described by eqs. 7 and 8, we derive and tabulate in Table 3 for each sight line the silicon depletion ($[\text{Si}/\text{H}]_{\text{dust}}$) and carbon depletion ($[\text{C}/\text{H}]_{\text{dust}}$) in dust from modeling its extinction curve. In Figure 21a we examine the correlation between $[\text{Si}/\text{H}]_{\text{dust}}$ and the strength of the 2175 Å extinction bump (c'_3). With a Pearson correlation coefficient of $R \approx -0.35$ and a Kendall $\tau \approx -0.23$ and $p \approx 0.02$, it is clear that the silicon depletion does not correlate with the 2175 Å bump. The possible relation between $[\text{C}/\text{H}]_{\text{dust}}$ and the extinction bump is evaluated in Figure 21b and no correlation is found ($R \approx 0.10$, $\tau \approx 0.04$ and $p \approx 0.68$). This can be understood in the context that, although the silicate-graphite model assigns the 2175 Å bump to graphite, the bulk carbon depletion is not consumed by the small graphite grains which are responsible for the extinction bump but by the submicron-sized graphite grains which, together with the submicron-sized silicate grains, account for the optical extinction. We have also explored the relation between $[\text{Si}/\text{H}]_{\text{dust}}$ and the strength of the nonlinear far-UV extinction rise (c'_4). As shown in Figure 21c, no correlation is found. Similarly, Figure 21d compares $[\text{C}/\text{H}]_{\text{dust}}$ with c'_4 and also reveals no correlation. We have also investigated how $[\text{Si}/\text{H}]_{\text{dust}}$ and $[\text{C}/\text{H}]_{\text{dust}}$ vary with R_V^{-1} . As shown in Figures 21e and f, neither $[\text{Si}/\text{H}]_{\text{dust}}$ nor $[\text{C}/\text{H}]_{\text{dust}}$ exhibits strong correlation with R_V^{-1} .

We now assess whether the dust depletions are generally consistent with the interstellar abundance constraints. For an interstellar dust model to be considered viable, the total abundance of element X ($[\text{X}/\text{H}]_{\text{tot}}$) implied by the dust model—the abundance of this element required to be tied up in dust ($[\text{X}/\text{H}]_{\text{dust}}$) plus the gas-phase abundance ($[\text{X}/\text{H}]_{\text{gas}}$)—should not exceed the interstellar abundance ($[\text{X}/\text{H}]_{\text{ISM}}$). Following Zuo et al. (2021) and Hensley & Draine (2021), we adopt the GCE-augmented protosolar abundances as the interstellar reference abundances (i.e., $[\text{C}/\text{H}]_{\text{ISM}} = 339 \pm 39$ ppm, $[\text{O}/\text{H}]_{\text{ISM}} = 589 \pm 68$ ppm, $[\text{Mg}/\text{H}]_{\text{ISM}} = 47.9 \pm 4.4$ ppm, $[\text{Si}/\text{H}]_{\text{ISM}} = 42.7 \pm 4.0$ ppm, and $[\text{Fe}/\text{H}]_{\text{ISM}} = 47.9 \pm 4.4$ ppm for the major dust-forming elements C, O, Mg, Si and Fe; see Table 1 in Zuo et al. 2021).

Figure 22 displays the measured gas-phase $[\text{C}/\text{H}]_{\text{gas}}$ abundances and the model-derived dust-phase $[\text{C}/\text{H}]_{\text{dust}}$ abundances of all the 16 sight lines for each of which $[\text{C}/\text{H}]_{\text{gas}}$ has been

observationally determined. The inferred total dust-plus-gas abundances $[C/H]_{\text{tot}}$ are compared with the interstellar abundance $[C/H]_{\text{ISM}}$ which is represented by the GCE-augmented protosolar C/H abundance. Although the majorities (10/16) of the sight lines are consistent with the interstellar abundance constraints (i.e., $[C/H]_{\text{tot}}$ does not surpass $[C/H]_{\text{ISM}}$ for 10 sight lines within the observational uncertainties of $[C/H]_{\text{gas}}$), six sight lines require $[C/H]_{\text{tot}}$ to exceed $[C/H]_{\text{ISM}}$. For these six sight lines with $[C/H]_{\text{tot}} > [C/H]_{\text{ISM}}$, the amount of C atoms available for making carbon dust are insufficient to account for that required by the observed extinction. This was known as the “C crisis” in the mid-1990s when the B star abundances were considered as the interstellar reference abundances (Snow & Witt 1995, 1996; also see Li 2005). Such a “C crisis” holds for these six sight lines even if we assume the GCE-augmented protosolar C abundance to be the interstellar C abundance. All these six sight lines are characterized by a relatively higher extinction-to-gas ratio of $A_V/N_H \gtrsim 5 \times 10^{-22} \text{ mag cm}^2 \text{ H}^{-1}$, while those sight lines with $[C/H]_{\text{tot}} \lesssim [C/H]_{\text{ISM}}$ all exhibit a lower extinction-to-gas ratio (i.e., $A_V/N_H < 5 \times 10^{-22} \text{ mag cm}^2 \text{ H}^{-1}$).³ Figure 22 also reveals a rough trend of increasing $[C/H]_{\text{gas}}$ with A_V/N_H . However, $[C/H]_{\text{gas}}$ does not appear to show any systematic variations with the hydrogen number density n_H .

The O/H depletion in dust is estimated from $[O/H]_{\text{dust}} \approx 4 \times [Si/H]_{\text{dust}}$ on the basis of the assumption of a stoichiometric composition of MgFeSiO_4 for silicate dust. Figure 23 displays the measured gas-phase $[O/H]_{\text{gas}}$ abundances and the model-derived dust-phase $[O/H]_{\text{dust}}$ abundances of all the 42 sight lines for each of which $[O/H]_{\text{gas}}$ has been observationally determined. While $[O/H]_{\text{gas}}$ varies from one sight line to another, there is no systematic variation of $[O/H]_{\text{gas}}$ with A_V/N_H or n_H . Most prominently, within the observational uncertainties of $[O/H]_{\text{gas}}$, $[O/H]_{\text{tot}}$ is in general agreement with $[O/H]_{\text{ISM}}$ for almost all sight lines. The only exceptions are the three sight lines toward HD 179406, BD+35 4258, and HD 73882 for which $[O/H]_{\text{tot}}$ is somewhat lower than $[O/H]_{\text{ISM}}$. This clearly shows that the vast majority (39/42) of the sight lines have no problem in accommodating the oxygen atoms missing from the gas phase, supporting our earlier finding based on a “gold” sample of 10 sight lines for which the gas-phase abundances of all the major dust-forming elements have been observationally measured (see Zuo et al. 2021). This is in stark contrast to the so-called “O crisis” – it has long been thought that in the ISM oxygen is heavily depleted from the gas phase and far exceeds (by as much as ~ 160 ppm of O/H) that can be accounted for by the main oxygen-containing refractory dust component such as silicates and oxides (see Jenkins 2009, Whittet 2010, Poteet et al. 2015). While Wang et al. (2015b) attributed

³HD 192639, the only sight line which has a high extinction-to-gas ratio ($A_V/N_H \approx 6.8 \times 10^{-22} \text{ mag cm}^2 \text{ H}^{-1}$) and does not violate the abundance constraints (i.e., $[C/H]_{\text{tot}} \lesssim [C/H]_{\text{ISM}}$), has a relatively low gas-phase abundance of $[C/H]_{\text{gas}} \approx 125$ ppm.

the excess O/H to μm -sized H_2O ice grains (which are large enough to suppress the $3.1\ \mu\text{m}$ absorption band of H_2O ice) and Potapov et al. (2020) attributed it to the trapping of H_2O ice in silicate grains, here in this work as well as in Zuo et al. (2021) we find that the dust depletions $[\text{O}/\text{H}]_{\text{dust}}$ inferred from the extinction combined with the gas-phase $[\text{O}/\text{H}]_{\text{gas}}$ are sufficient in fully accommodating the interstellar O/H for the vast majority (39/42) of the sight lines.

Figure 24 compares the interstellar $[\text{Si}/\text{H}]_{\text{ISM}}$ abundances with the measured gas-phase $[\text{Si}/\text{H}]_{\text{gas}}$ abundances and the model-derived dust-phase $[\text{Si}/\text{H}]_{\text{dust}}$ abundances and their combinations $[\text{Si}/\text{H}]_{\text{tot}}$ of all the 48 sight lines for each of which $[\text{Si}/\text{H}]_{\text{gas}}$ has been observationally determined. While most of the sight lines are highly depleted in silicon, there are several sight lines in which $[\text{Si}/\text{H}]_{\text{gas}}$ is rich and accounts for $\gtrsim 1/3$ of the interstellar $[\text{Si}/\text{H}]_{\text{ISM}}$. Also, there is no systematic variation of $[\text{Si}/\text{H}]_{\text{gas}}$ with A_V/N_{H} or n_{H} . For most (43/48) of the sight lines, we find $[\text{Si}/\text{H}]_{\text{tot}}$ substantially exceeds $[\text{Si}/\text{H}]_{\text{ISM}}$, implying that there are not enough silicon atoms to make the silicate dust required to account for the observed extinction. Figure 24 also shows that $[\text{Si}/\text{H}]_{\text{tot}}$ tends to increase with A_V/N_{H} , indicating that the shortage of Si/H becomes more severe in sight lines with a higher extinction-to-gas ratio.

Figure 25 displays the measured gas-phase $[\text{Mg}/\text{H}]_{\text{gas}}$ abundances and the model-derived dust-phase $[\text{Mg}/\text{H}]_{\text{dust}}$ abundances of all the 38 sight lines for each of which $[\text{Mg}/\text{H}]_{\text{gas}}$ has been observationally determined. Although it is widely believed that magnesium is almost fully depleted from the gas phase, there are appreciable amounts ($[\text{Mg}/\text{H}]_{\text{gas}} \gtrsim 5$ ppm) of gaseous magnesium atoms in essentially all the 38 sight lines. The gas-phase $[\text{Mg}/\text{H}]_{\text{gas}}$ abundances vary from one sight line to another, but does not show any systematic variations with A_V/N_{H} or n_{H} . Figure 25 also compares the interstellar abundance $[\text{Mg}/\text{H}]_{\text{ISM}}$ with the total dust-plus-gas abundances $[\text{Mg}/\text{H}]_{\text{tot}}$ inferred from the extinction modeling, revealing that $\sim 40\%$ of the sight lines require $[\text{Mg}/\text{H}]_{\text{tot}} > [\text{Mg}/\text{H}]_{\text{ISM}}$ and most of these sight lines are characterized by a higher extinction-to-gas ratio (i.e., $A_V/N_{\text{H}} > 4.8 \times 10^{-22} \text{ mag cm}^2 \text{ H}^{-1}$).

Figure 26 compares the interstellar $[\text{Fe}/\text{H}]_{\text{ISM}}$ abundances with the measured gas-phase $[\text{Fe}/\text{H}]_{\text{gas}}$ abundances and the model-derived dust-phase $[\text{Fe}/\text{H}]_{\text{dust}}$ abundances and their combinations $[\text{Fe}/\text{H}]_{\text{tot}}$ of all the 21 sight lines for each of which $[\text{Fe}/\text{H}]_{\text{gas}}$ has been observationally determined. Unlike silicon and magnesium of which the gas-phase abundances are unnegligible in the sight lines studied here, iron is essentially completely depleted from the gas phase in the 21 sight lines displayed in Figure 26, independent with A_V/N_{H} or n_{H} . While the majority of the sight lines have $[\text{Fe}/\text{H}]_{\text{tot}} \lesssim [\text{Fe}/\text{H}]_{\text{ISM}}$, $\sim 1/3$ of the sight lines require more iron than available to form silicate dust in order to account for the observed extinction.

To summarize, for those sight lines with $A_V/N_{\text{H}} \lesssim 4.8 \times 10^{-22} \text{ mag cm}^2 \text{ H}^{-1}$, the in-

terstellar C/H, Si/H, Mg/H and Fe/H abundances approximated by the GCE-augmented protosolar abundances are sufficient to account for the gas-phase abundances observationally measured and the dust-phase abundances derived from the observed extinction. However, for those sight lines with $A_V/N_H \gtrsim 4.8 \times 10^{-22} \text{ mag cm}^2 \text{ H}^{-1}$, there are shortages of C, Si, Mg and Fe elements for forming the dust to account for the observed extinction. It is interesting to note that such an A_V/N_H ratio is close to that recently derived for the Galactic ISM (e.g., $A_V/N_H \approx 4.6 \times 10^{-22} \text{ mag cm}^2 \text{ H}^{-1}$ for the “gold” sample of Zuo et al. (2021), $A_V/N_H \approx 4.8 \times 10^{-22} \text{ mag cm}^2 \text{ H}^{-1}$ of Zhu et al. (2017) for a large sample of sight lines toward supernova remnants, planetary nebulae, and X-ray binaries), although a nominal extinction-to-gas ratio of $A_V/N_H \approx 5.3 \times 10^{-22} \text{ mag cm}^2 \text{ H}^{-1}$ is commonly adopted for the diffuse ISM. A much lower ratio of $A_V/N_H \approx 3.5 \times 10^{-22} \text{ mag cm}^2 \text{ H}^{-1}$ was derived by Lenz et al. (2017), for diffuse, low-column-density regions with $N(\text{HI}) < 4 \times 10^{20} \text{ H cm}^{-2}$. Perhaps the interstellar gas is not well mixed as previously assumed so that the interstellar abundances of heavy elements may actually have regional variations. If this is true, a universal A_V/N_H ratio is not expected. Indeed, very recently De Cia et al. (2021) found large variations in metallicity over a factor of 10 in the local Galactic ISM.

Finally, we explore how the mean grain sizes derived in §3 from fitting the observed extinction curves vary with R_V^{-1} . Let $\langle a \rangle_{\text{sil}}$ and $\langle a \rangle_{\text{gra}}$ respectively be the mean sizes of the silicate and graphite grains, each weighted by grain area, grain mass, or V -band extinction cross section [$C_{\text{ext}}(a, \lambda_V)$]. We also derive the “overall mean grain size” as the average of $\langle a \rangle_{\text{sil}}$ and $\langle a \rangle_{\text{gra}}$, weighted by the mass fraction of each dust component in the same manner as described in §6 of Mishra & Li (2017). Our results closely resemble that of Mishra & Li (2017; see their Figures 14, 15): the area-, mass-, and $C_{\text{ext}}(a, \lambda_V)$ -weighted mean grain sizes all anti-correlate with R_V^{-1} . This clearly shows that *denser* regions of *larger* R_V values, on an average, are characterized by *larger* grains. The underlying physics could be related to the rotational disruption of dust driven by radiative torques which depends on the local conditions such as gas density and starlight intensity (see Hoang 2019, 2021).

5. Summary

We have synthesized and modeled the extinction curves of a large number of Galactic sight lines from the near-IR to the far-UV for which the gas-phase abundances of at least one of the major dust-forming elements (i.e., C, O, Si, Mg, and Fe) have been observationally determined. Our principal results are as follows:

1. The extinction curves of all sight lines except HD 93222 are closely reproduced from the far-UV to the near-IR by a simple mixture of silicate dust and graphite dust. The

extinction curve of the sight line toward HD 93222 is rather abnormal. Despite a large $R_V = 4.76$, it exhibits a sharp 2175 Å extinction bump and a steep far-UV rise at $\lambda^{-1} > 5.9 \mu\text{m}^{-1}$ which are both characteristic of diffuse regions with $R_V < 3.1$.

2. The gas-phase $[\text{C}/\text{H}]_{\text{gas}}$ and $[\text{O}/\text{H}]_{\text{gas}}$ abundances vary from one sight line to another, but do not show any systematic variations with the hydrogen number density n_{H} . While $[\text{C}/\text{H}]_{\text{gas}}$ appears to increase with the extinction-to-gas ratio A_V/N_{H} , $[\text{O}/\text{H}]_{\text{gas}}$ does not show any systematic variations with A_V/N_{H} .
3. While there are appreciable amounts of gas-phase Mg and Si atoms in the sight lines studied here, Fe is essentially completely depleted from the gas phase. Like $[\text{O}/\text{H}]_{\text{gas}}$, $[\text{Mg}/\text{H}]_{\text{gas}}$ and $[\text{Si}/\text{H}]_{\text{gas}}$ vary from one sight line to another, but do not show any systematic variations with A_V/N_{H} or n_{H} .
4. For those sight lines with $A_V/N_{\text{H}} \lesssim 4.8 \times 10^{-22} \text{ mag cm}^2 \text{ H}^{-1}$, the interstellar C/H, Si/H, Mg/H and Fe/H abundances approximated by the protosolar abundances augmented by Galactic chemical evolution are sufficient to account for the gas-phase abundances observationally measured and the dust-phase abundances derived from the observed extinction. In contrast, for those sight lines with $A_V/N_{\text{H}} \gtrsim 4.8 \times 10^{-22} \text{ mag cm}^2 \text{ H}^{-1}$, there are shortages of C, Si, Mg and Fe elements for making dust to account for the observed extinction.
5. While it is generally believed that in the diffuse ISM a substantial fraction of the oxygen atoms remain unaccounted for in interstellar gas and dust, it is found that, for the majority of the lines of sight studied here, there does not appear to be a “missing oxygen” problem, i.e., the interstellar oxygen atoms are fully accommodated by gas and dust.

WBZ and GZ are supported in part by the NSFC grants No. 11988101 and No. 11890694 as well as the National Key R&D Program of China (No. 2019YFA0405502) and the CSST Milky Way Survey project. We thank Dr. B.T. Draine, Dr. A. Mishra, Dr. A.N. Witt and the anonymous referee for very helpful discussions and suggestions.

REFERENCES

- Allamandola, L.J., Tielens, A.G.G.M., & Barker, J.R. 1985, ApJ, 290, L25
- André, M., Oliveira, C., Howk, J. C., et al. 2003, ApJ, 591, 1000

- Bohren, C.F., & Huffman, D.R. 1983, *Absorption and Scattering of Light by Small Particles* (New York: Wiley)
- Cardelli, J. A., & Clayton, G. C. 1991, *AJ*, 101, 1021
- Cardelli, J. A., Clayton, G., C., & Mathis, J. S. 1989, *ApJ*, 345, 245
- Cardelli, J. A., Meyer, D. M., Jura, M., et al. 1996, *ApJ*, 467, 334
- Cardelli, J. A., & Savage, B. D. 1988, *ApJ*, 325, 864
- Cartledge, S. I. B., Meyer, D. M., & Lauroesch, J. T. 2003, *ApJ*, 597, 408
- Cartledge, S. I. B., Lauroesch, J. T., Meyer, D. M., & Sofia, U. J. 2004, *ApJ*, 613, 1037
- Cartledge, S. I. B., Lauroesch, J. T., Meyer, D. M., & Sofia, U. J. 2006, *ApJ*, 641, 327
- Cartledge, S. I. B., Lauroesch, J. T., Meyer, D. M., et al. 2008, *ApJ*, 687, 1043
- Crinklaw, G., Federman, S. R., & Joseph, C. L. 1994, *ApJ*, 424, 748
- Cui, J., Bechtold, J., Ge, J., & Meyer, D. M. 2005, *ApJ*, 633, 649
- De Cia, A., Jenkins, E. B., Fox, A. J., et al. 2021, *Nature*, 597, 206
- Désert, F.-X., Boulanger, F., & Puget, J. L. 1990, *A&A*, 500, 313
- Diplas, A., & Savage, B. D. 1994, *ApJS*, 93, 211
- Draine, B.T., & Lee, H.M. 1984, *ApJ*, 258, 89D
- Federman, S. R., Strom, C. J., Lambert, D. L., et al. 1994, *ApJ*, 424, 772
- Fitzpatrick, E.L., & Massa, D. 1990, *ApJS*, 72, 163 (FM90)
- Fitzpatrick, E.L., & Massa, D. 2007, *ApJ*, 663, 320
- Fitzpatrick, E. L., Massa, D., Gordon, K. D., et al. 2019, *ApJ*, 886, 108
- Gnaciński, P., & Krogulec, M. 2006, *Acta Astron.*, 56, 373
- Gordon, K.D., Cartledge, S., & Clayton, G.C. 2009, *ApJ*, 705, 1320
- Hanson, M. M., Snow, T. P., & Black, J. H. 1992, *ApJ*, 392, 571
- Hensley, B. S., & Draine, B. T. 2017, *ApJ*, 836, 179

- Hensley, B. S. & Draine, B. T. 2021, ApJ, 906, 73
- Hoang, T. 2019, ApJ, 876, 13
- Hoang, T. 2021, ApJ, 907, 37
- Hoang, T., Vinh, N.-A., & Quynh Lan, N. 2016, ApJ, 824, 18
- Jenkins, E.B. 2009, ApJ, 700, 1299
- Jenkins, E.B. 2019, ApJ, 872,55
- Jenkins, E. B., Savage, B. D., & Spitzer, L. 1986, ApJ, 301, 355
- Jensen, A. G., Rachford, B. L., & Snow, T. P. 2005, ApJ, 619, 891
- Jensen, A. G., Rachford, B. L., & Snow, T. P. 2007, ApJ, 654, 955
- Jensen, A. G., & Snow, T. P. 2007a, ApJ, 669, 378
- Jensen, A. G., & Snow, T. P. 2007b, ApJ, 669, 401
- Jensen, A. G., Snow, T. P., Sonneborn, G., et al. 2010, ApJ, 711, 1236
- Jones, A. P., Fanciullo, L., Köhler, M., et al. 2013, A&A, 558, A62
- Kimura, H., Mann, I., & Jessberger, E. K. 2003a, ApJ, 582, 846
- Kimura, H., Mann, I., & Jessberger, E. K. 2003b, ApJ, 583, 314
- Knauth, D. C., Meyer, D. M., & Lauroesch, J. T. 2006, ApJ, 647, L115
- Larson, K. A., Whittet, D. C. B., & Hough, J. H. 1996, ApJ, 472, 755
- Léger, A., & Puget, J. 1984, A&A, 137, L5
- Lenz, D., Hensley, B. S., & Doré, O. 2017, ApJ, 846, 38
- Li, A. 2004, in ASP Conf. Ser. 309, Astrophysics of Dust, ed. A. N. Witt, G. C. Clayton, & B. T. Draine (San Francisco, CA: ASP), 417
- Li, A. 2005, ApJ, 622, 965
- Li, A. 2020, Nature Astronomy, 4, 339
- Li, A., & Draine, B.T. 2001a, ApJ, 554, 778

- Li, A., & Draine, B.T. 2001b, ApJL, 550, L213
- Li, A., & Greenberg, J.M. 1997, A&A, 323, 566
- Li, A., & Greenberg, J.M. 1998, A&A, 339, 591
- Lodders, K. 2003, ApJ, 591, 1220
- Mathis, J. S. 1996, ApJ, 472, 643
- Mathis, J.S., Ruml, W., & Nordsieck, K.H. 1977, ApJ, 217, 425
- Mazzei, P., & Barbaro, G. 2011, A&A, 527, A34
- Meyer, D. M., Jura, M., & Cardelli, J. A. 1998, ApJ, 493, 222
- Miller, A., Lauroesch, J. T., Sofia, U. J., et al. 2007, ApJ, 659, 441
- Mishra, A., & Li, A. 2015, ApJ, 809, 120
- Mishra, A., & Li, A. 2017, ApJ, 850, 138
- Parvathi V. S., Sofia U. J., Murthy J., et al. 2012, ApJ, 760, 36
- Potapov, A., Bouwman, J., Jäger, C., et al. 2021, Nature Astronomy, 5, 78
- Poteet, C. A., Whittet, D. C. B., & Draine, B. T. 2015, ApJ, 801, 110
- Press, W.H., Teukolsky, S.A., Vetterling, W.T., & Flannery, B.P. 1992, Numerical Recipes in FORTRAN: The Art of Scientific Computing (2nd ed.; Cambridge: Cambridge Univ. Press)
- Rachford, B. L., Snow, T. P., Tumlinson, J., et al. 2002, ApJ, 577, 221
- Rachford, B. L., Snow, T. P., Destree, J. D., et al. 2009, ApJS, 180, 125
- Sheffer, Y., Rogers, M., Federman, S. R., et al. 2007, ApJ, 667, 1002
- Sheffer, Y., Rogers, M., Federman, S. R., et al. 2008, ApJ, 687, 1075
- Siebenmorgen, R., & Krügel, E. 1992, A&A, 259, 614
- Siebenmorgen, R., Voshchinnikov, N. V., Bagnulo, S., et al. 2018, A&A, 611, A5
- Snow, T.P., & Witt, A.N. 1995, Science, 270, 1455
- Snow, T.P., & Witt, A.N. 1996, ApJ, 468, L65

Snow, T. P., Rachford, B. L., & Figoski, L. 2002, *ApJ*, 573, 662

Sofia, U.J., & Meyer, D.M. 2001, *ApJ*, 554, L221

Sofia, U. J., Cardelli, J. A., & Savage, B. D. 1994, *ApJ*, 430, 650

Sofia, U. J., Lauroesch, J. T., Meyer, D. M., et al. 2004, *ApJ*, 605, 272

Sofia, U. J., Parvathi, V. S., Babu, B. R. S., et al. 2011, *AJ*, 141, 22

Sonnentrucker, P., Friedman, S. D., Welty, D. E., et al. 2003, *ApJ*, 596, 350

van Steenberg, M. E., & Shull, J. M. 1988, *ApJS*, 67, 225

Valencic, L. A., Clayton, G. C., & Gordon, K. D. 2004, *ApJ*, 616, 912

Voshchinnikov, N. V., & Henning, Th. 2010, *A&A*, 517, A45

Wang, S., Li, A., & Jiang, B. W. 2015a, *ApJ*, 811, 38 (WLJ15)

Wang, S., Li, A., & Jiang, B. W. 2015b, *MNRAS*, 454, 569

Weingartner, J.C., & Draine, B.T. 2001, *ApJ*, 548, 296 (WD01)

Welty, D. E., & Crowther, P. A. 2010, *MNRAS*, 404, 1321

Welty, D. E. & Fowler, J. R. 1992, *ApJ*, 393, 193

Whittet, D. C. B. 1984, *MNRAS*, 210, 479

Whittet, D. C. B. 2010, *ApJ*, 710, 1009

Witt, A. N., Bohlin, R. C., & Stecher, T. P. 1984, *ApJ*, 279, 698

Zhu, H., Tian, W., Li, A., & Zhang, M.F. 2017, *MNRAS*, 471, 3494

Zubko, V., Dwek, E., & Arendt, R. G. 2004, *ApJS*, 152, 211

Zuo, W. B., Li, A., & Zhao, G. 2021, *ApJS*, 252, 22

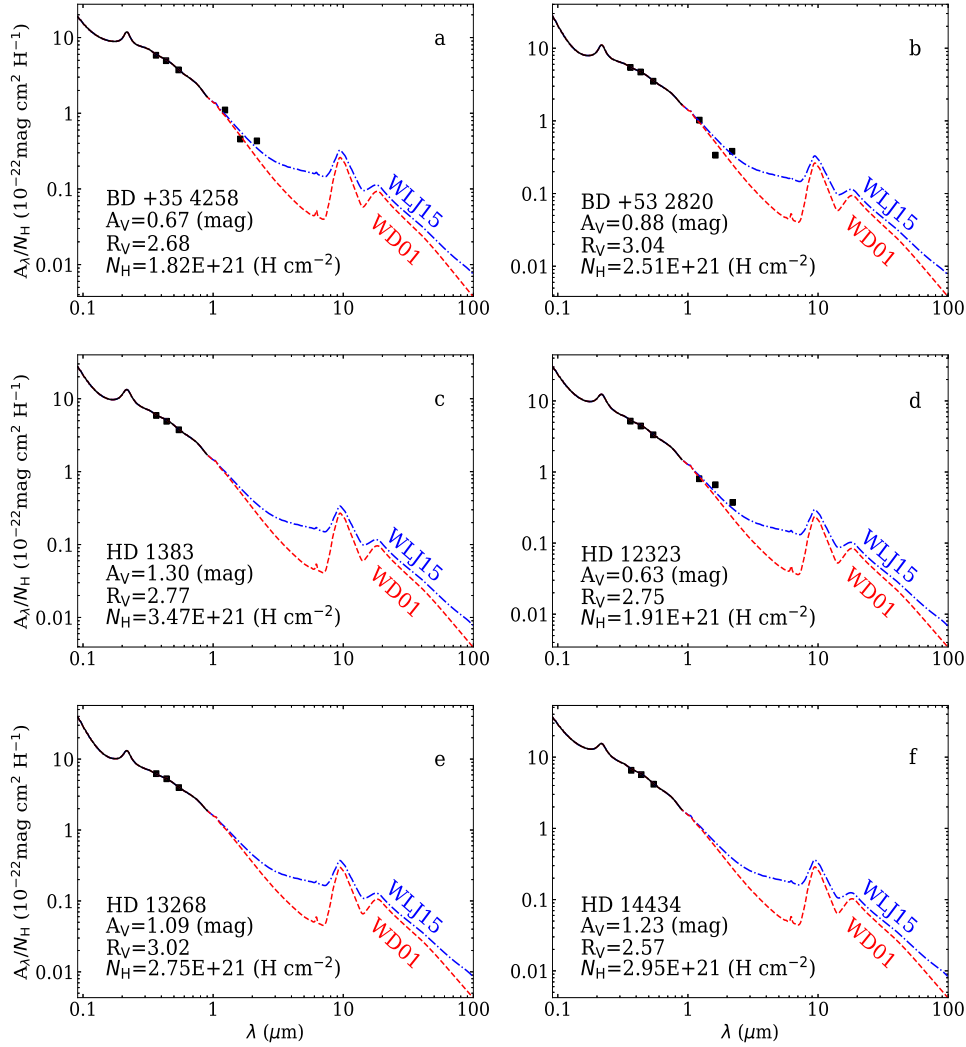


Fig. 1.— Interstellar extinction curves from the far-UV to the far-IR for the lines of sight toward BD+35 4258 (a), BD+53 2820 (b), HD 1383 (c), HD 12323 (d), HD 13268 (e) and HD 14434 (f), with the FM curve for $\lambda^{-1} > 3.3 \mu\text{m}^{-1}$, the CCM curve for $1.1 \mu\text{m}^{-1} < \lambda^{-1} < 3.3 \mu\text{m}^{-1}$, and the $R_V = 3.1$ model curves of Weingartner & Draine (2001; red dashed line) and Wang, Li & Jiang (2015a; blue dot-dashed line) for $0.9 \mu\text{m} < \lambda < 1 \text{ cm}$. Whenever available, U, B, V, J, H, and K broadband photometric extinction data (see Table 1) are shown as black squares.

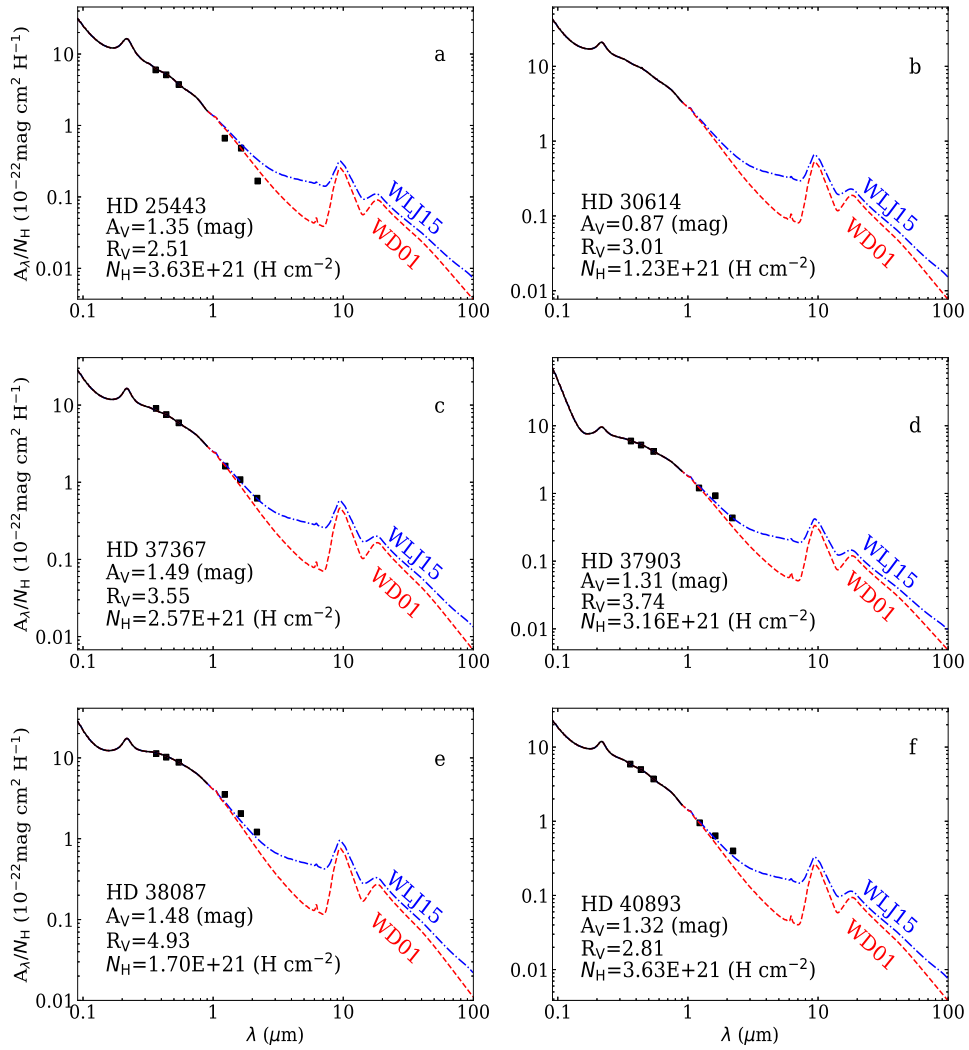


Fig. 2.— Same as Figure 1 but for HD 25443 (a), HD 30614 (b), HD 37367 (c), HD 37903 (d), HD 38087 (e), and HD 40893 (f).

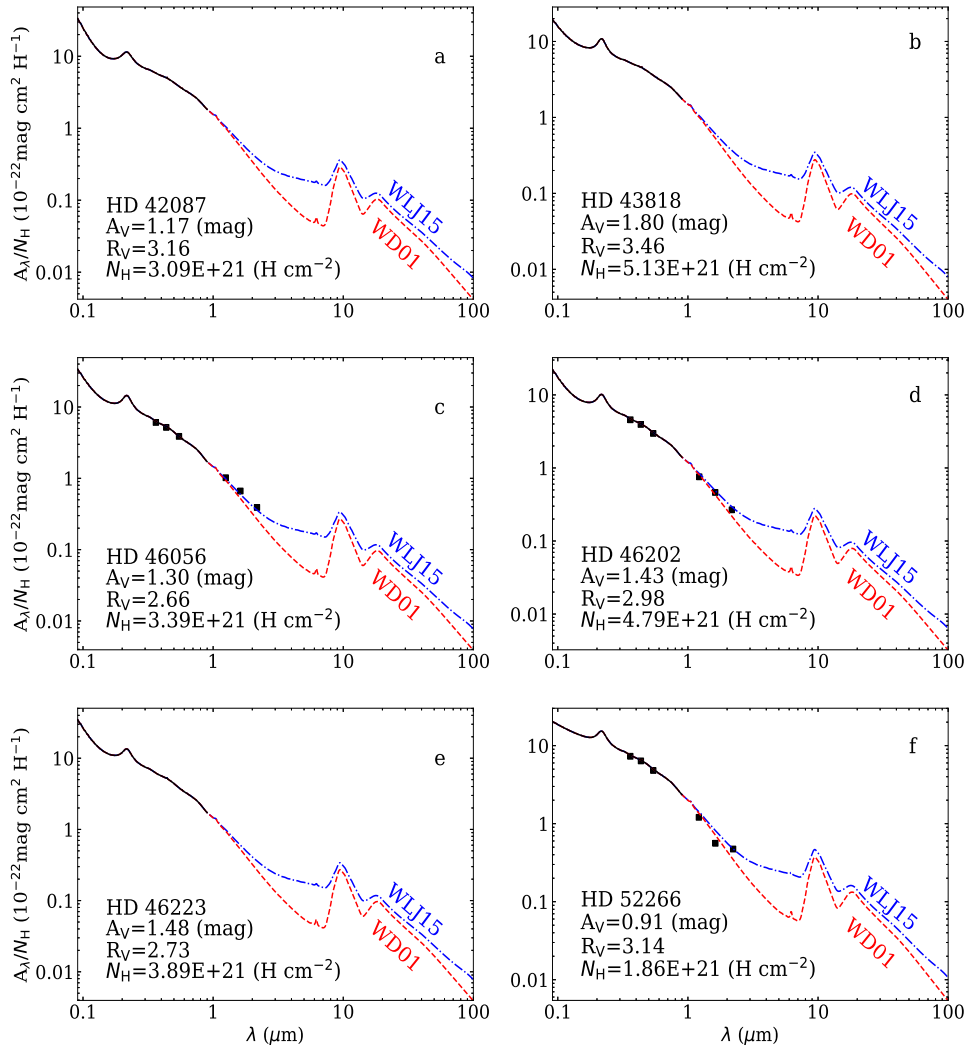


Fig. 3.— Same as Figure 1 but for HD 42087 (a), HD 43818 (b), HD 46056 (c), HD 46202 (d), HD 46223 (e), and HD 52266 (f).

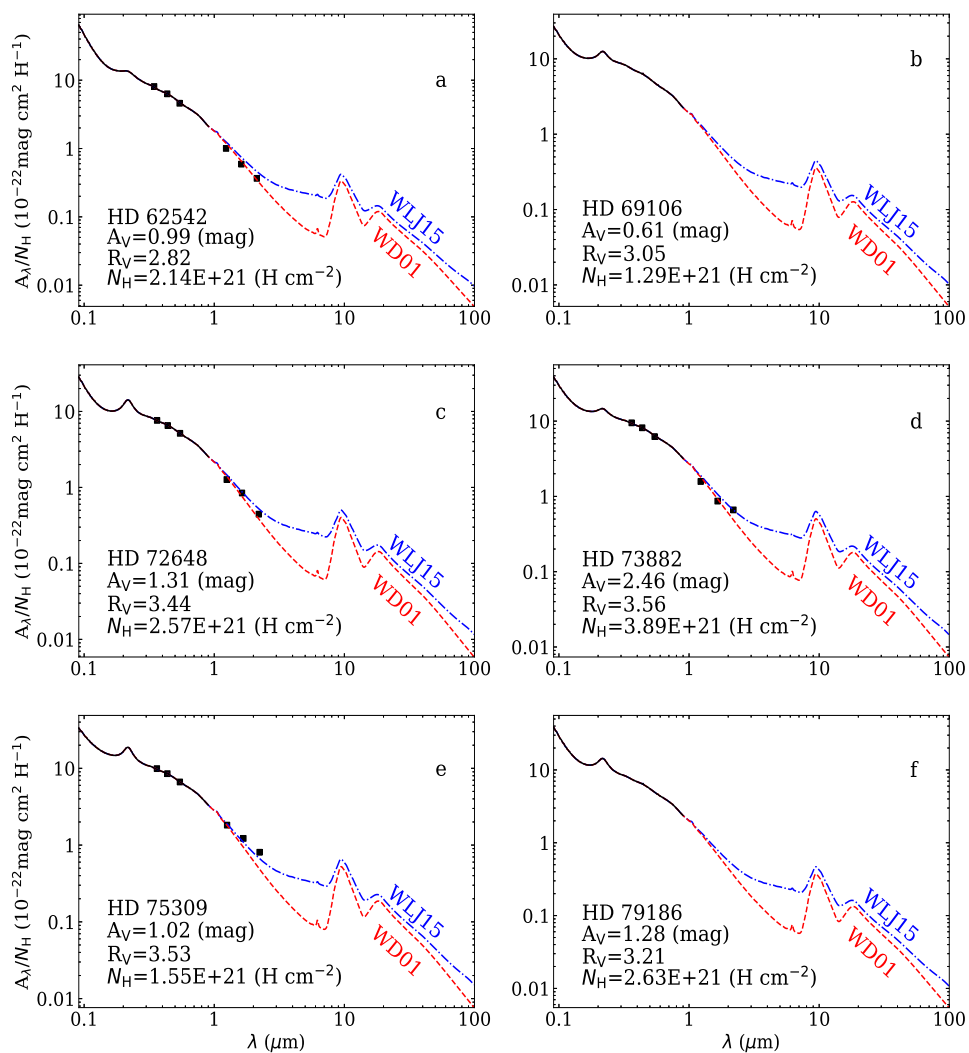


Fig. 4.— Same as Figure 1 but for HD 62542 (a), HD 69106 (b), HD 72648 (c), HD 73882 (d), HD 75309 (e), and HD 79186 (f).

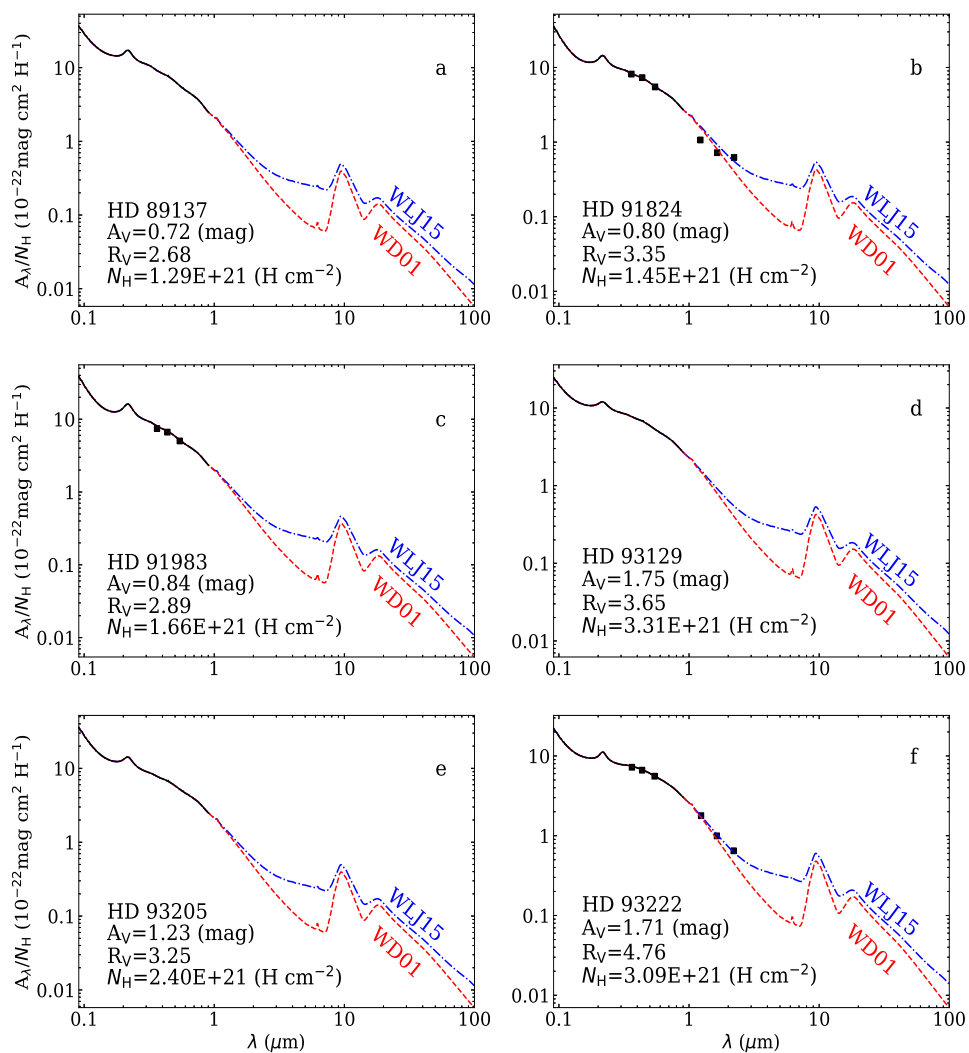


Fig. 5.— Same as Figure 1 but for HD 89137 (a), HD 91824 (b), HD 91983 (c), HD 93129 (d), HD 93205 (e), and HD 93222 (f).

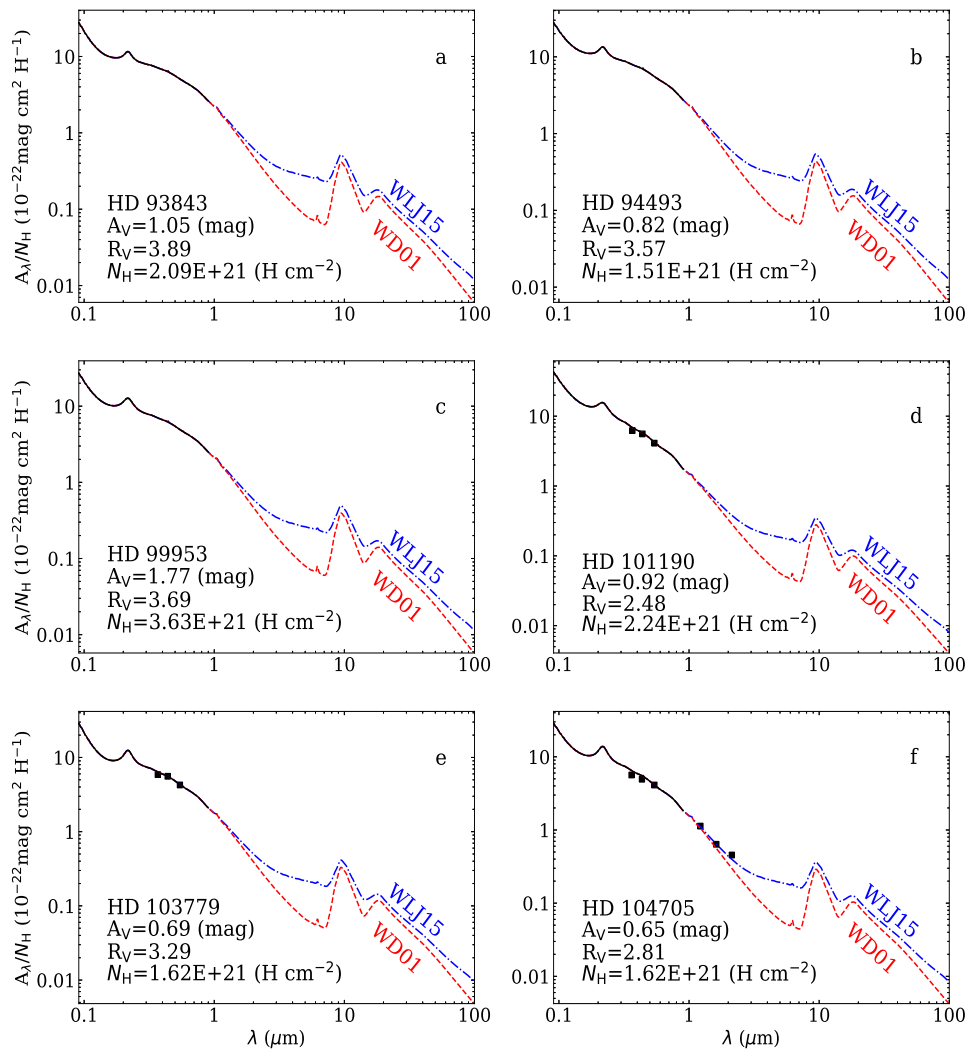


Fig. 6.— Same as Figure 1 but for HD 93843 (a), HD 94493 (b), HD 99953 (c), HD 101190 (d), HD 103779 (e), and HD 104705 (f).

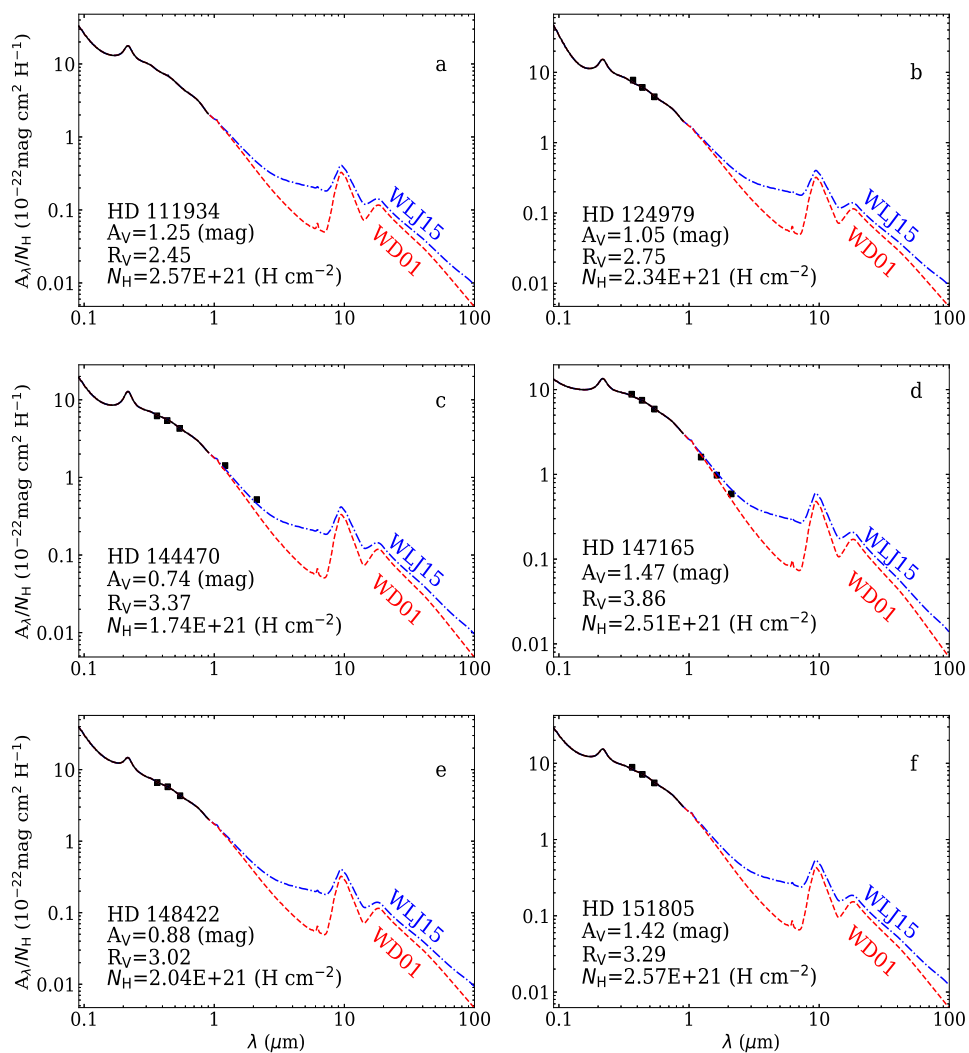


Fig. 7.— Same as Figure 1 but for HD 111934 (a), HD 124979 (b), HD 144470 (c), HD 147165 (d), HD 148422 (e), and HD 151805 (f).

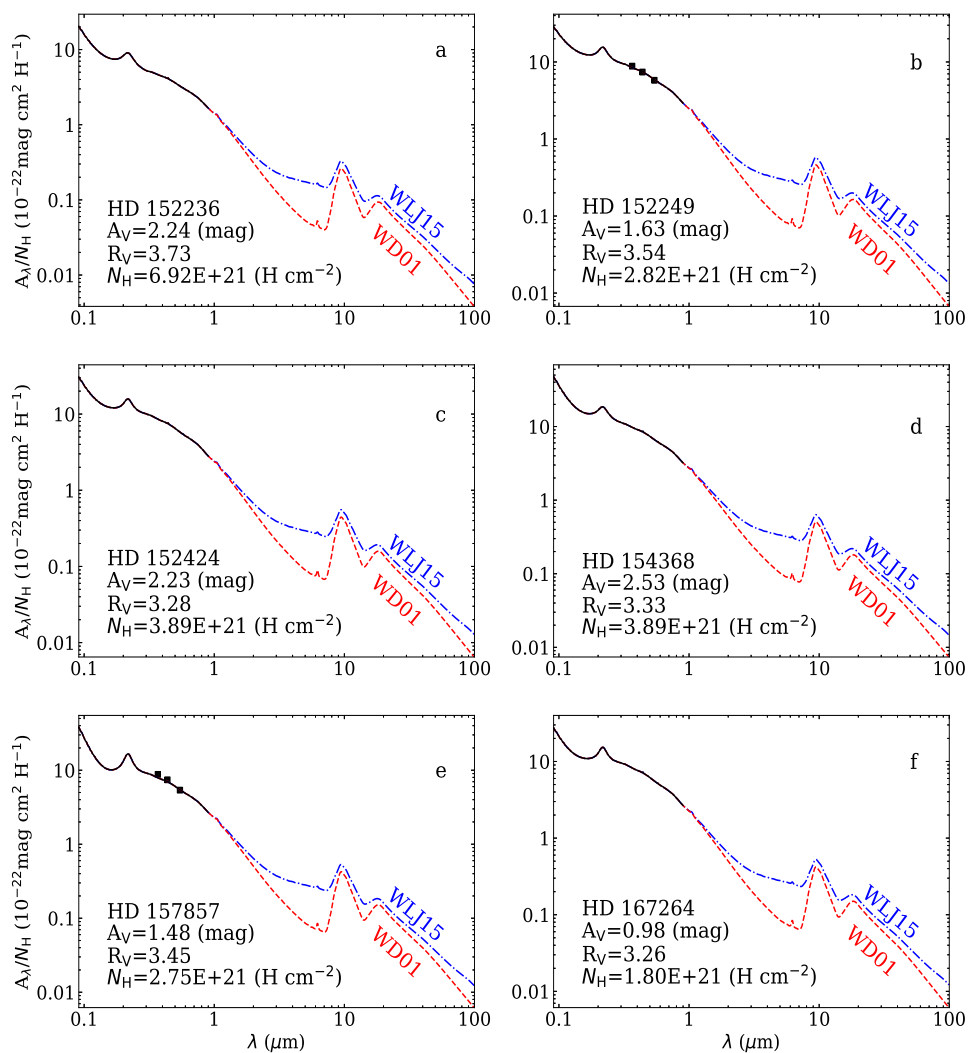


Fig. 8.— Same as Figure 1 but for HD 152236 (a), HD 152249 (b), HD 152424 (c), HD 154368 (d), HD 157857 (e), and HD 167264 (f).

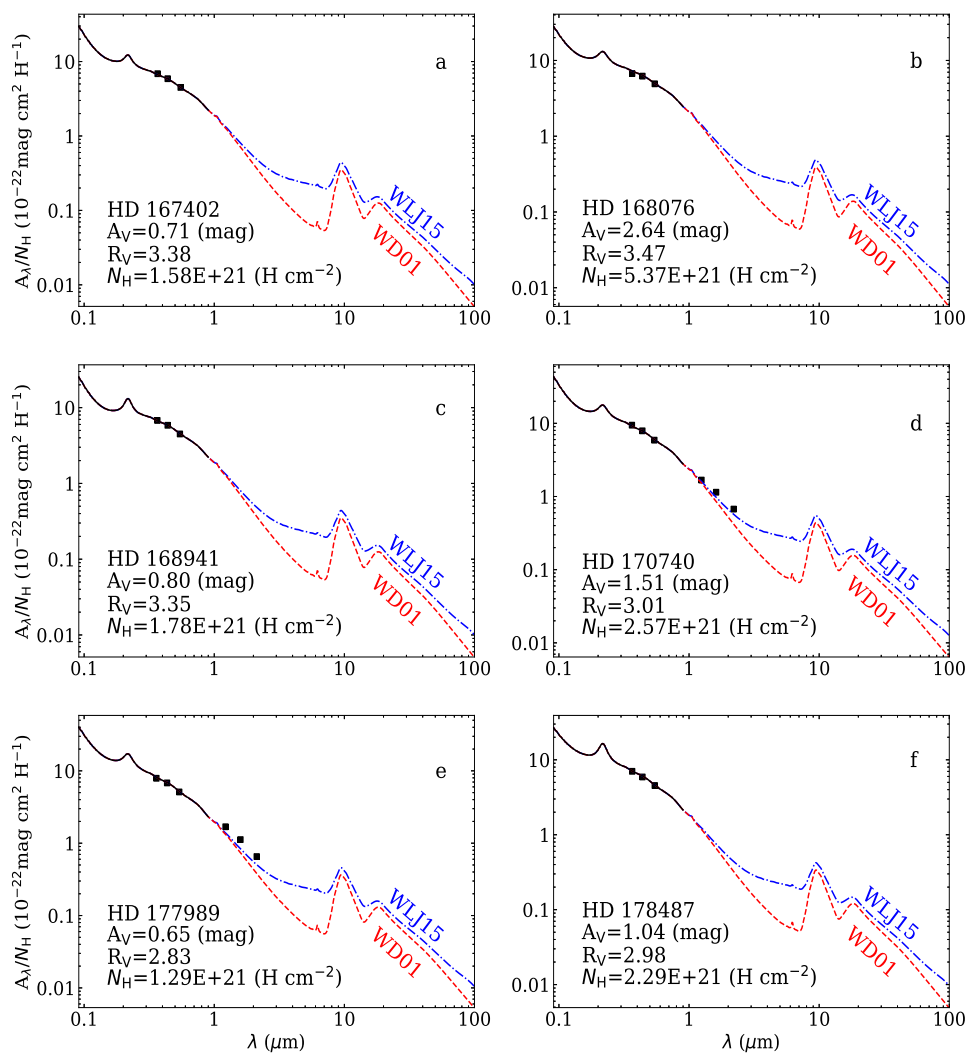


Fig. 9. — Same as Figure 1 but for HD 167402 (a), HD 168076 (b), HD 168941 (c), HD 170740 (d), HD 177989 (e), and HD 178487 (f).

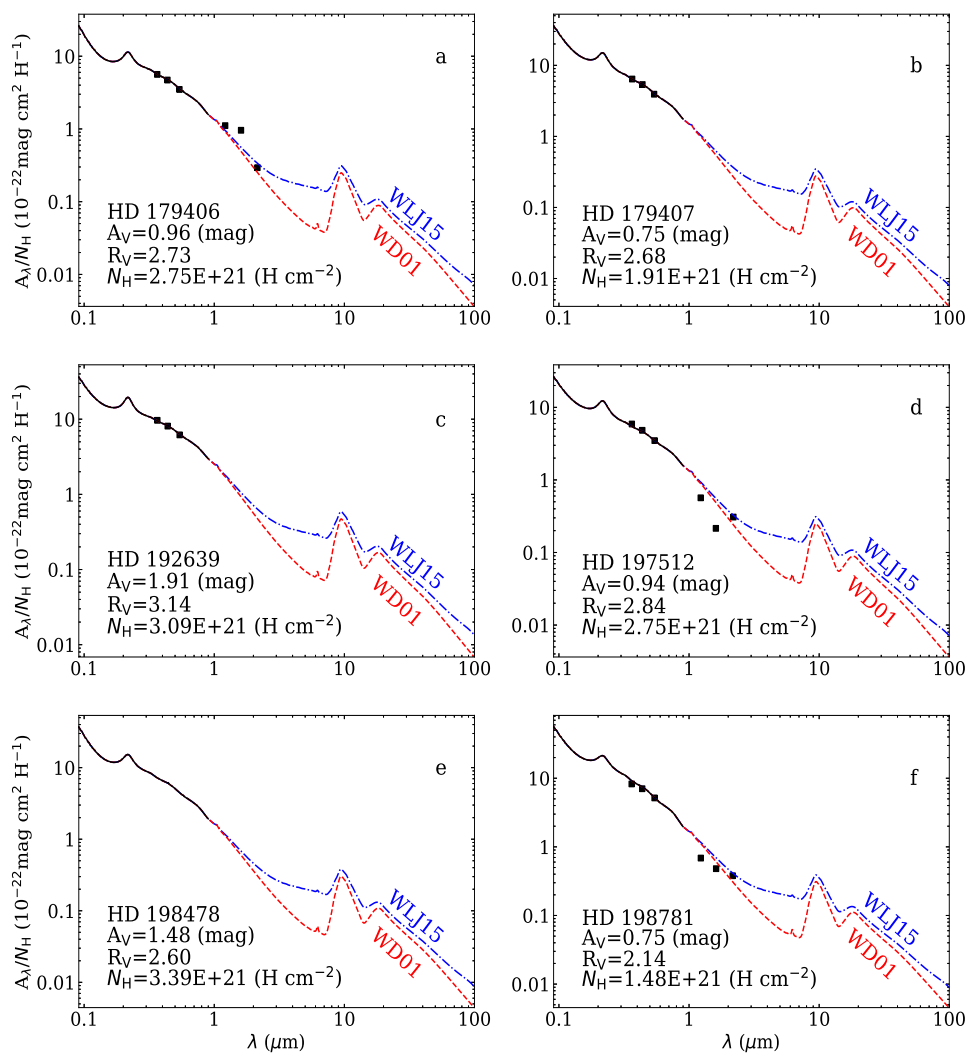


Fig. 10.— Same as Figure 1 but for HD 179406 (a), HD 179407 (b), HD 192639 (c), HD 197512 (d), HD 198478 (e), and HD 198781 (f).

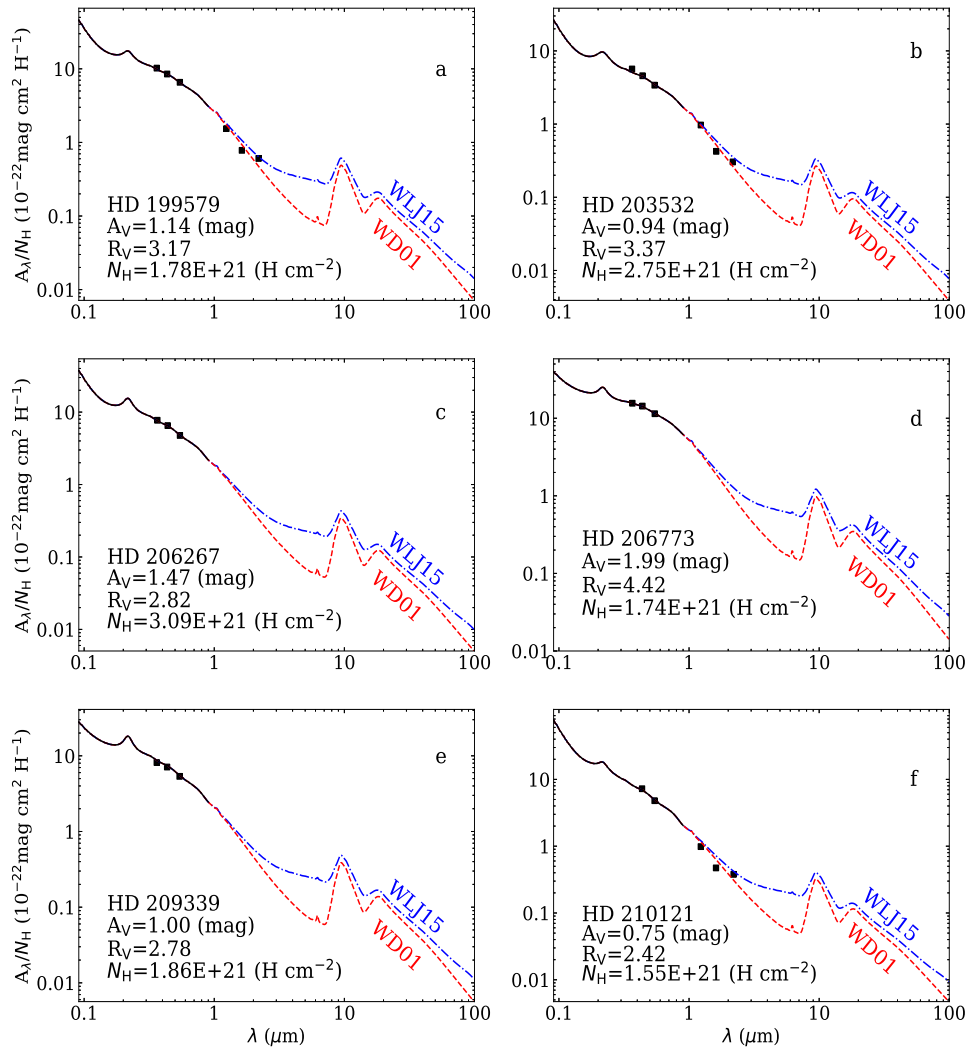


Fig. 11.— Same as Figure 1 but for HD 199579 (a), HD 203532 (b), HD 206267 (c), HD 206773 (d), HD 209339 (e), and HD 210121 (f).

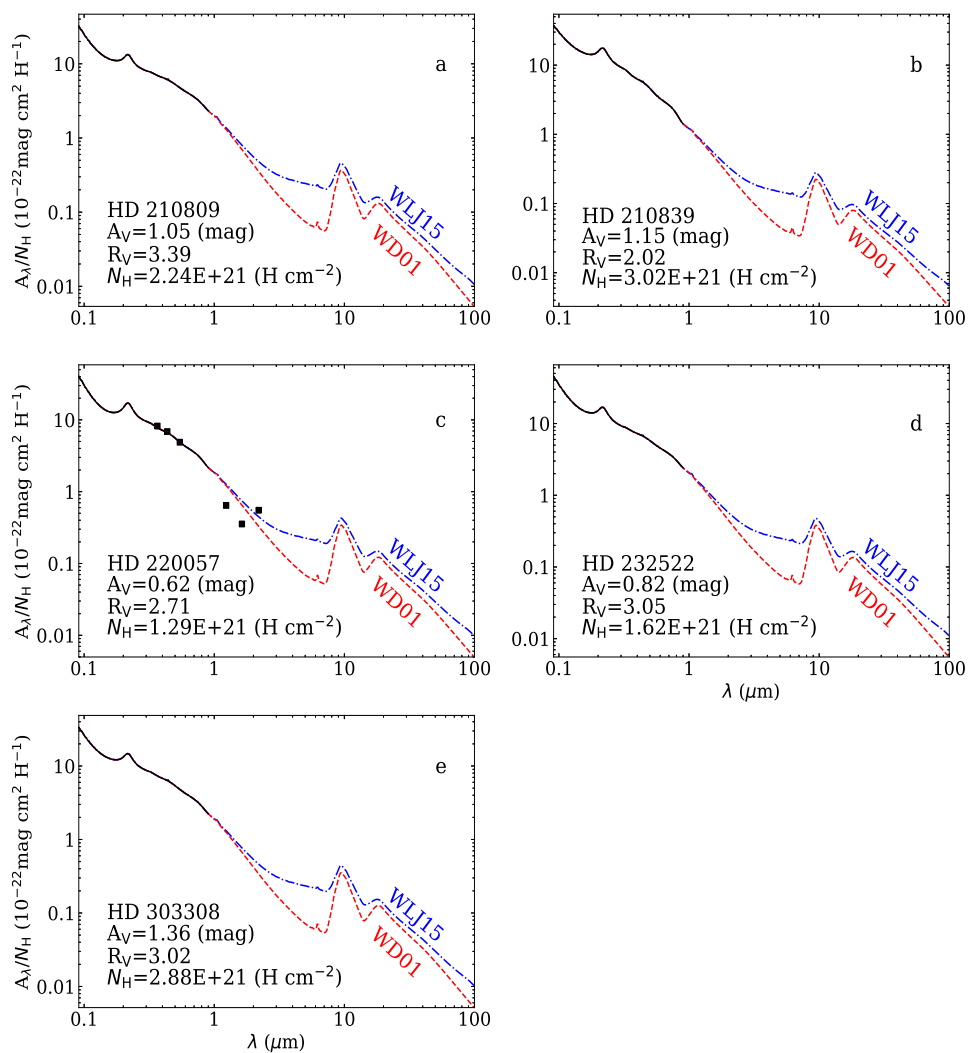


Fig. 12.— Same as Figure 1 but for HD 210809 (a), HD 210839 (b), HD 220057 (c), HD 232522 (d), and HD 303308 (e).

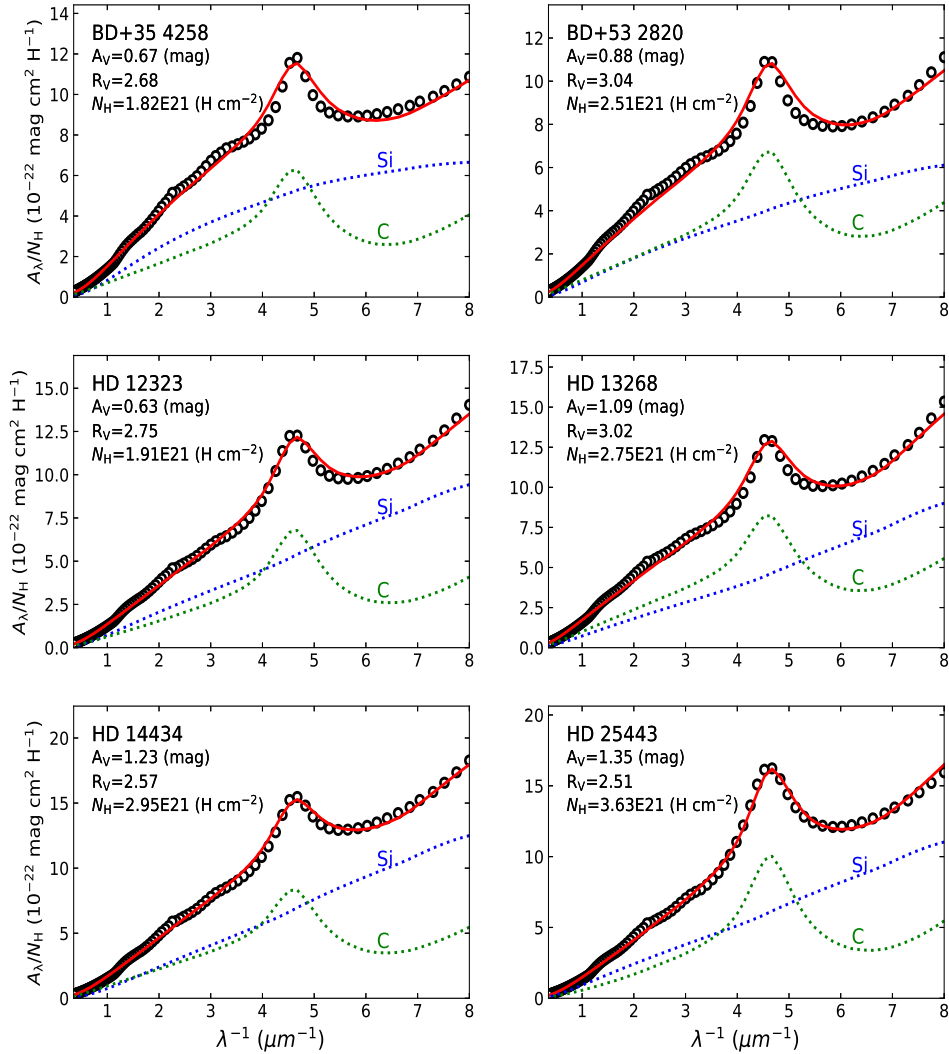


Fig. 13.— Fitting the extinction curves of BD+35 4258, BD+53 2820, HD 12323, HD 13268, HD 14434, and HD 25443. The observed extinction curves (open black circles), as described in §2 and shown in Figures 1–12, are represented by the FM90 parameterization at $\lambda^{-1} > 3.3 \mu\text{m}^{-1}$, by the CCM parameterization at $1.1 < \lambda^{-1} < 3.3 \mu\text{m}^{-1}$, and by the WLJ15 model curve at $\lambda^{-1} < 1.1 \mu\text{m}^{-1}$ (or by the WD01 model curve if it agrees better with the J, H, K extinction data). The solid red line plots the model extinction curve which is a combination of amorphous silicate (dotted green line, labeled “Si”) and graphite (dashed blue line, labeled “C”).

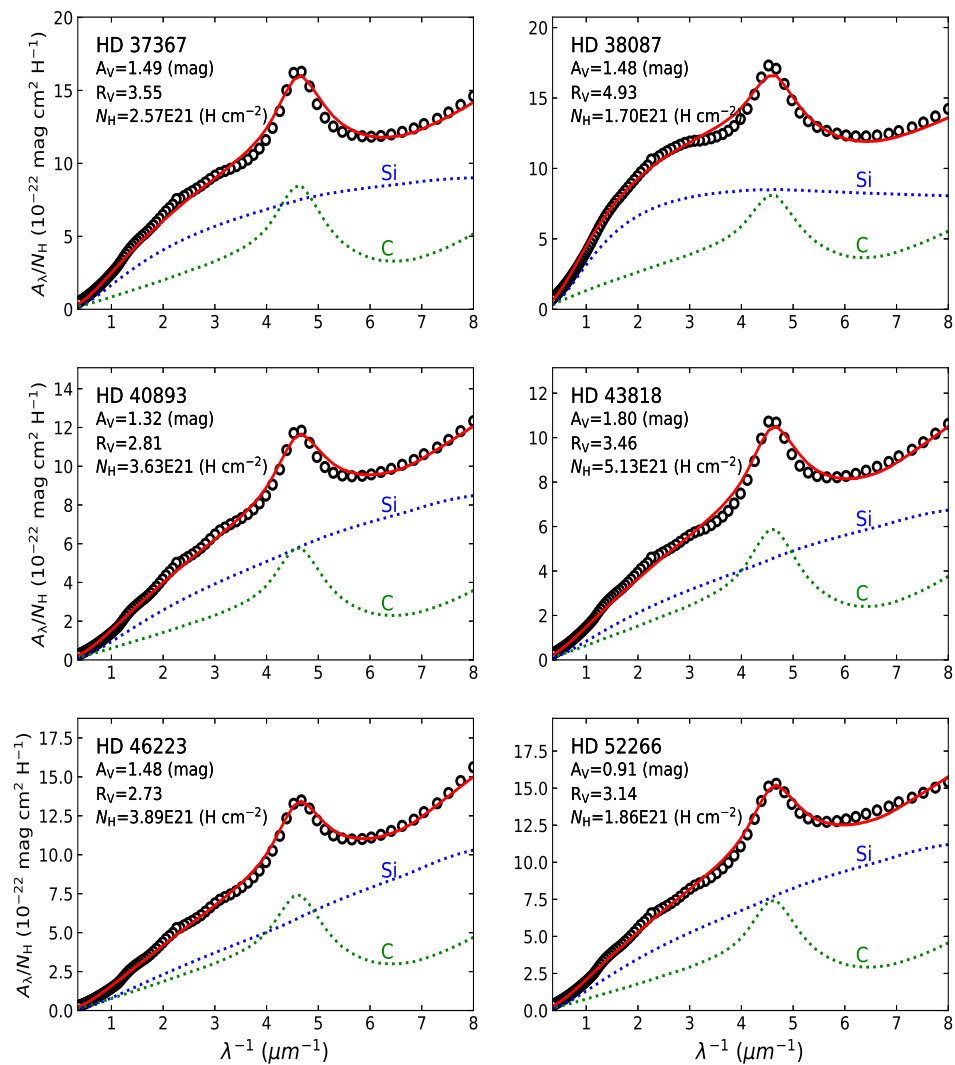


Fig. 14.— Same as Figure 13, but for HD 37367, HD 38087, HD 40893, HD 43818, HD 46223, and HD 52266.

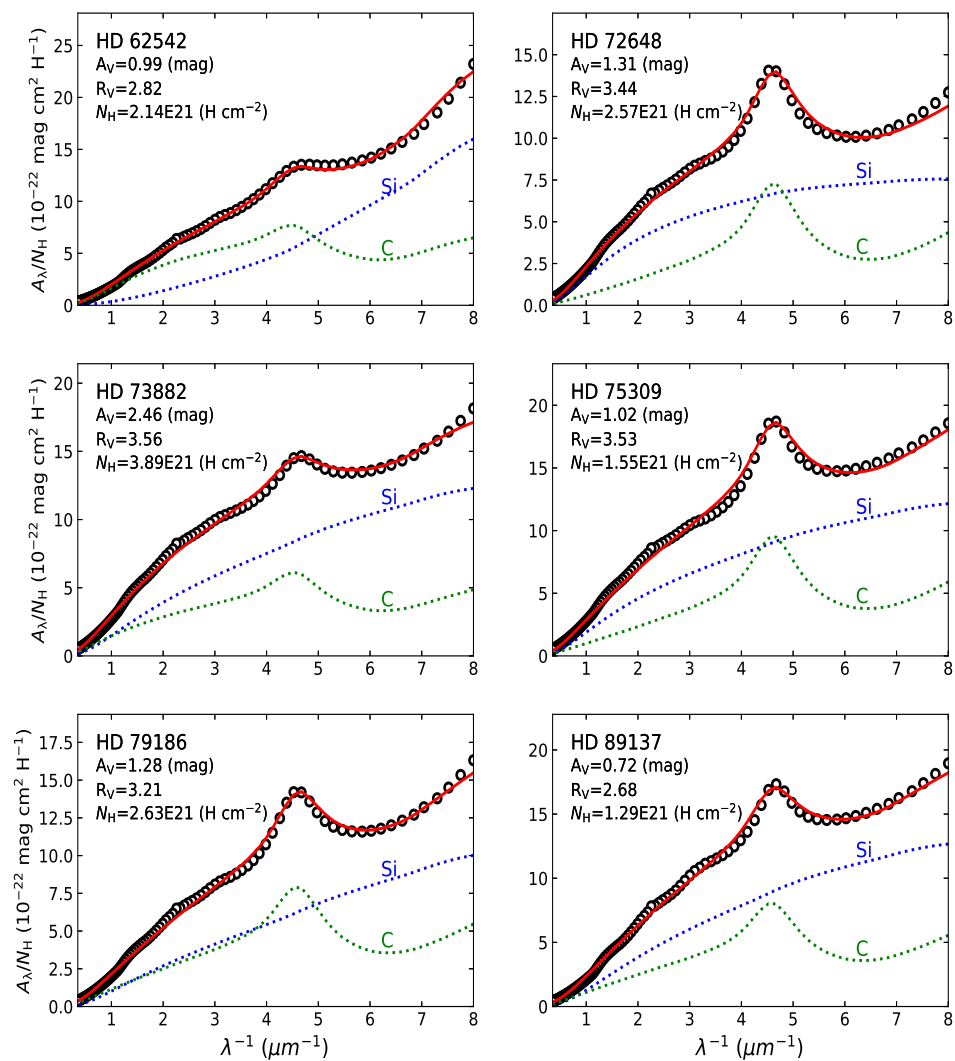


Fig. 15.— Same as Figure 13, but for HD 62542, HD 72648, HD 73882, HD 75309, HD 79186, and HD 89137.

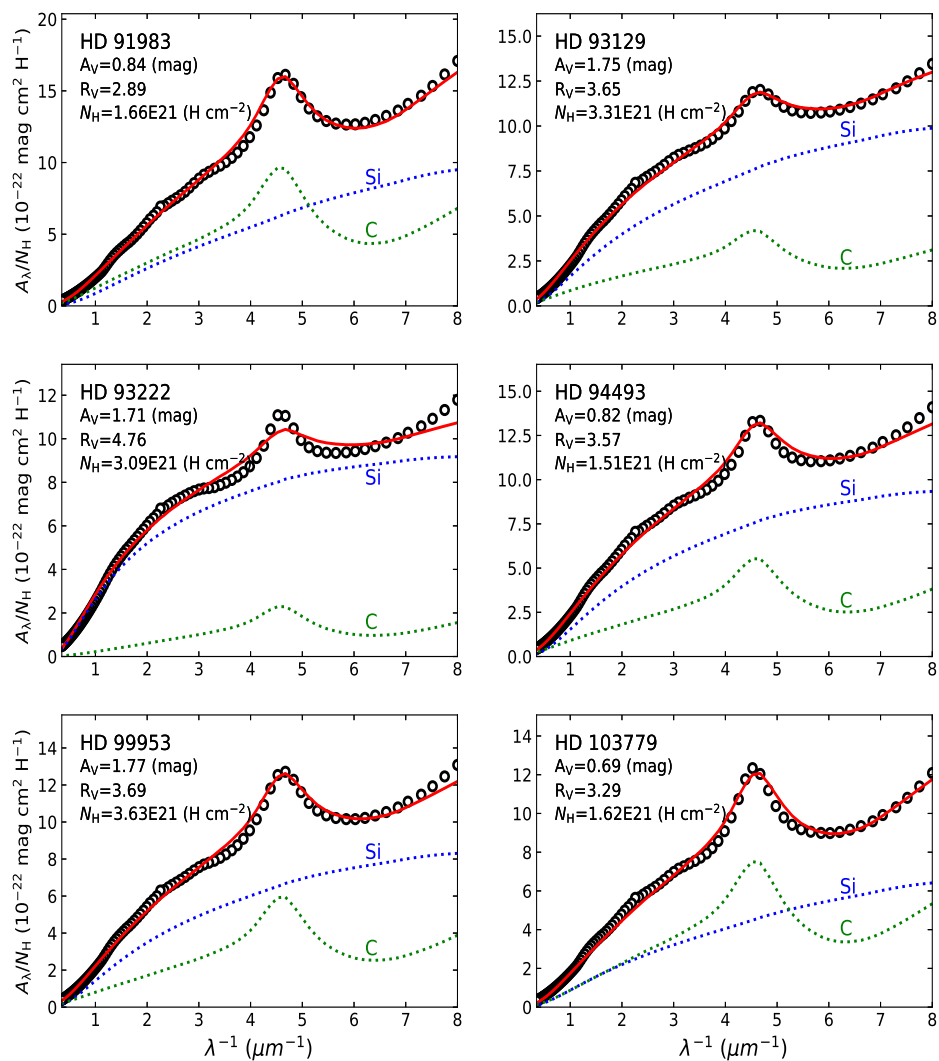


Fig. 16.— Same as Figure 13, but for HD 91983, HD 93129, HD 93222, HD 94493, HD 99953, and HD 103779.

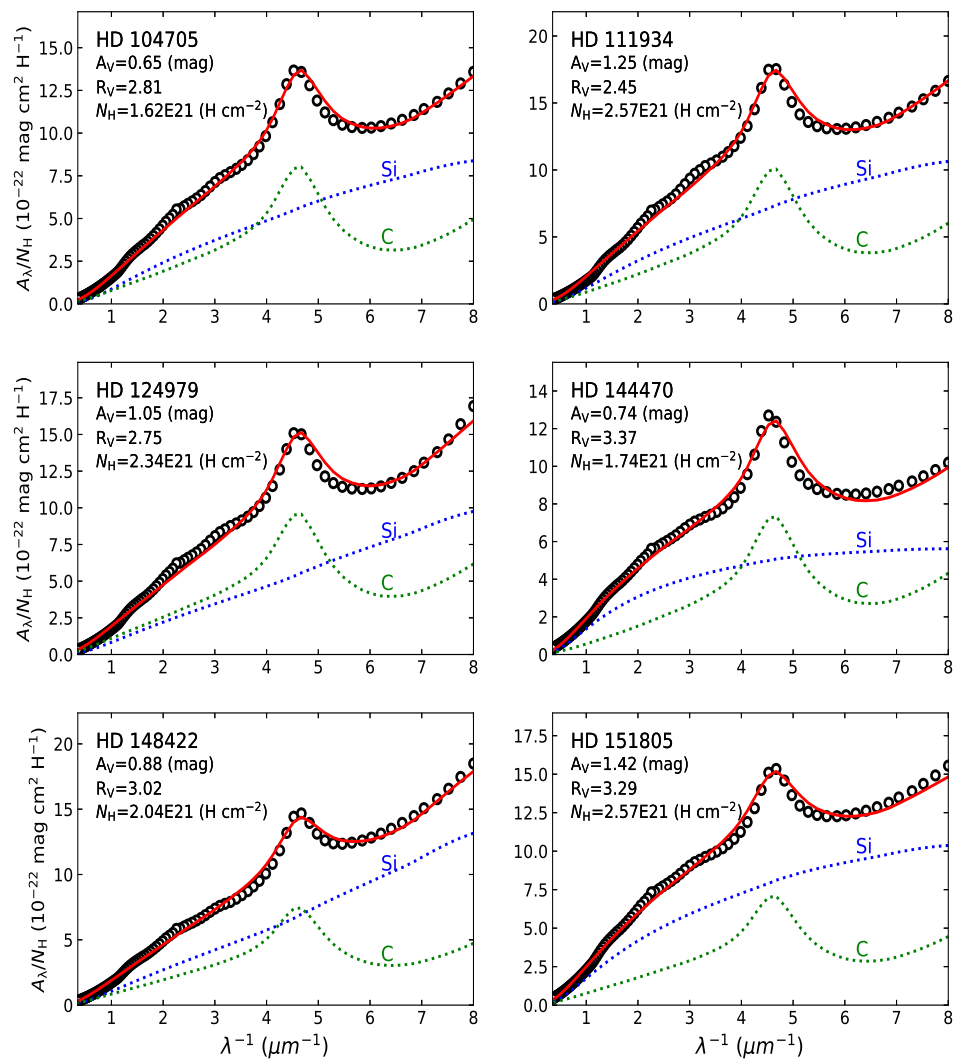


Fig. 17.— Same as Figure 13, but for HD 104705, HD 111934, HD 124979, HD 144470, HD 148422, and HD 151805.

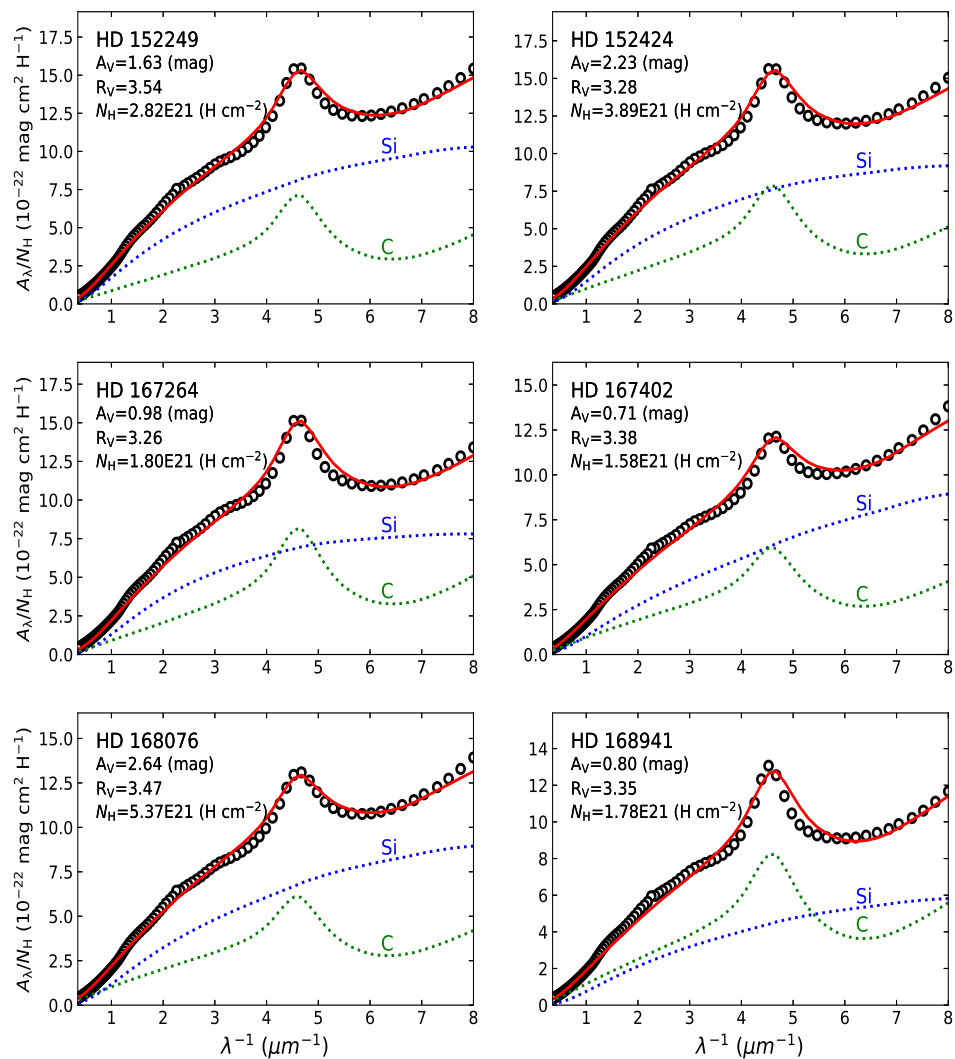


Fig. 18.— Same as Figure 13, but for HD 152249, HD 152424, HD 167264, HD 167402, HD 168076, and HD 168941.

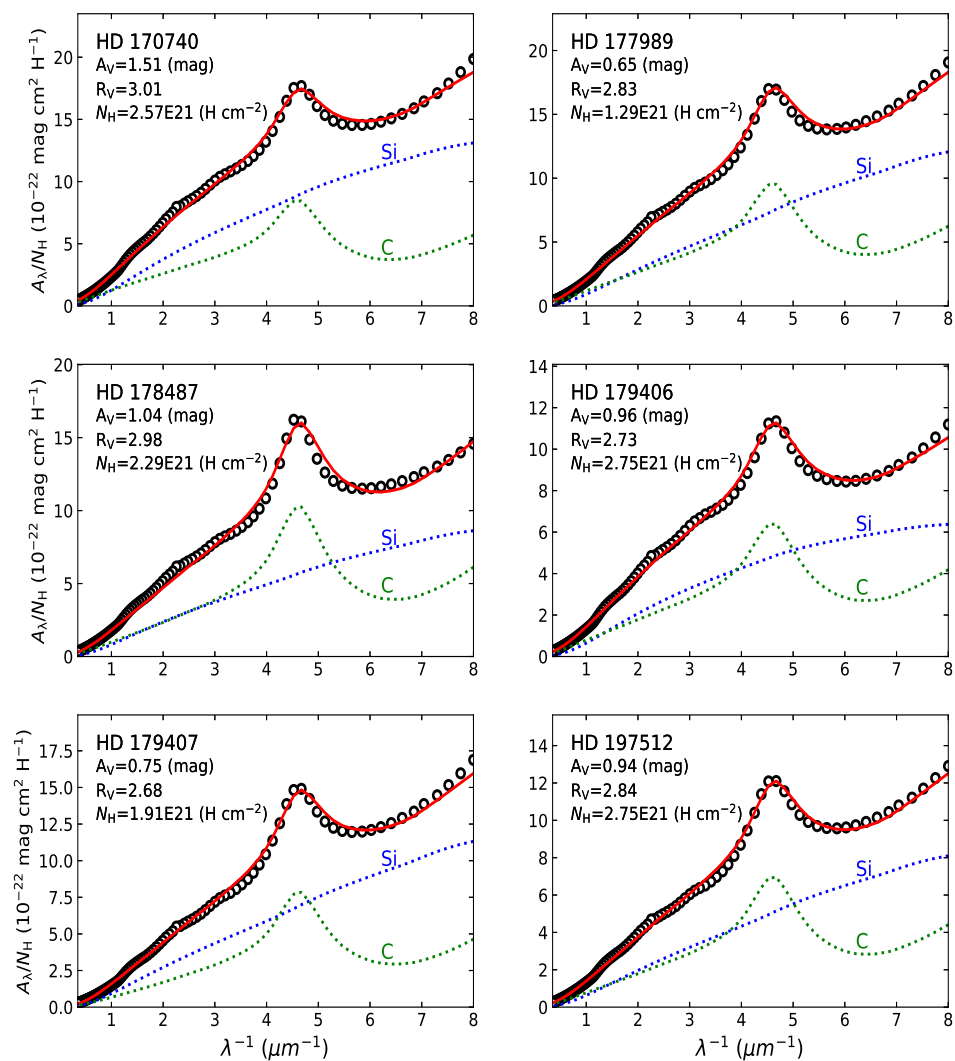


Fig. 19.— Same as Figure 13, but for HD 170740, HD 177989, HD 178487, HD 179406, HD 179407, and HD 197512.

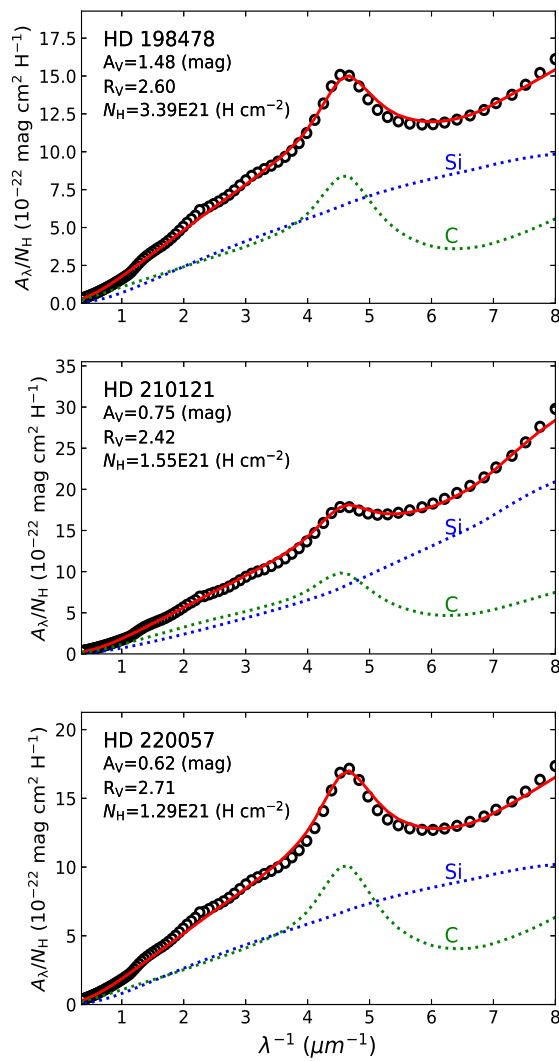


Fig. 20.— Same as Figure 13, but for HD 198478, HD 210121, and HD 220057.

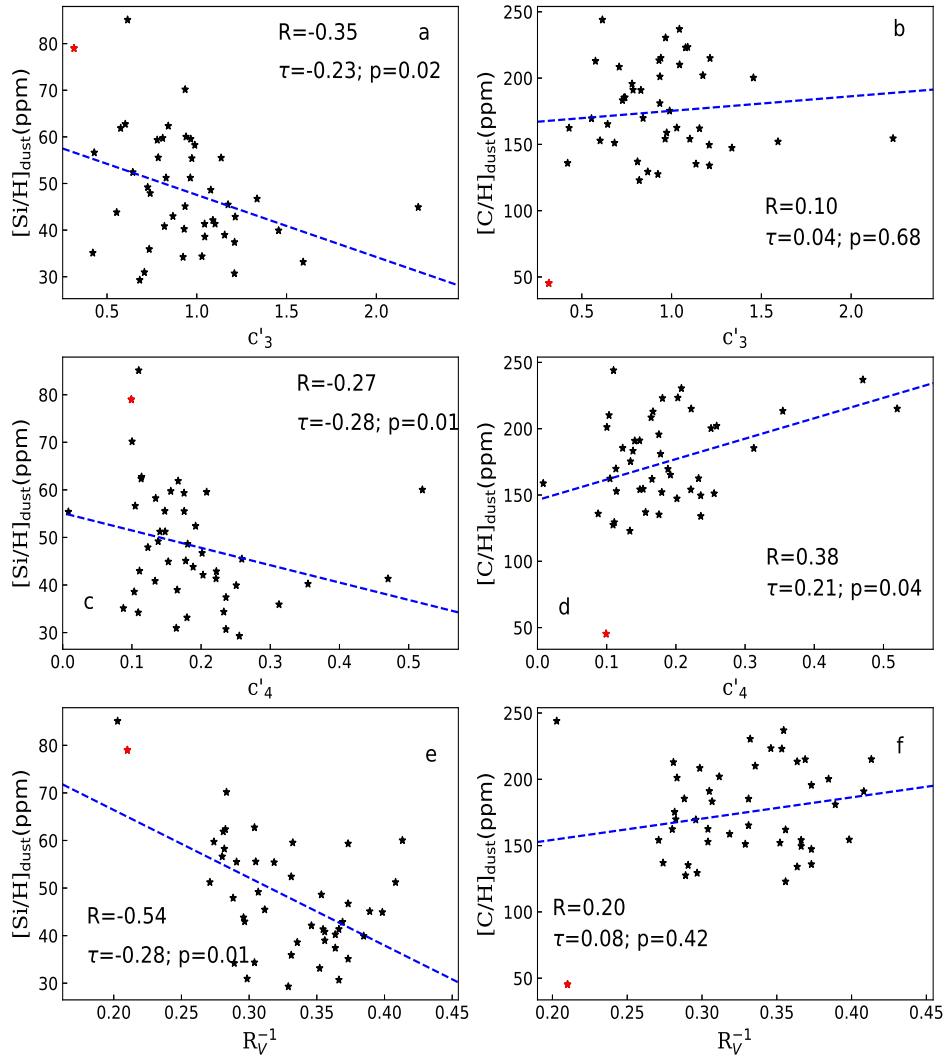


Fig. 21.— Upper panel: Correlation diagrams between the 2175 Å bump (c'_3) and the silicon depletion $[\text{Si}/\text{H}]_{\text{dust}}$ (a) or the carbon depletion $[\text{C}/\text{H}]_{\text{dust}}$ (b) derived from fitting the extinction curve of each sightline with a mixture of amorphous silicate dust and graphite dust. Middle panel: The correlations between the far-UV nonlinear extinction rise (c'_4) and $[\text{Si}/\text{H}]_{\text{dust}}$ (c) or $[\text{C}/\text{H}]_{\text{dust}}$ (d). Lower panel: The correlations between R_V^{-1} and $[\text{Si}/\text{H}]_{\text{dust}}$ (e) or $[\text{C}/\text{H}]_{\text{dust}}$ (f). In each panel, HD 93222 is shown as a red star for which neither the 2175 Å bump nor the far-UV rise is well reproduced (see Figure 16).

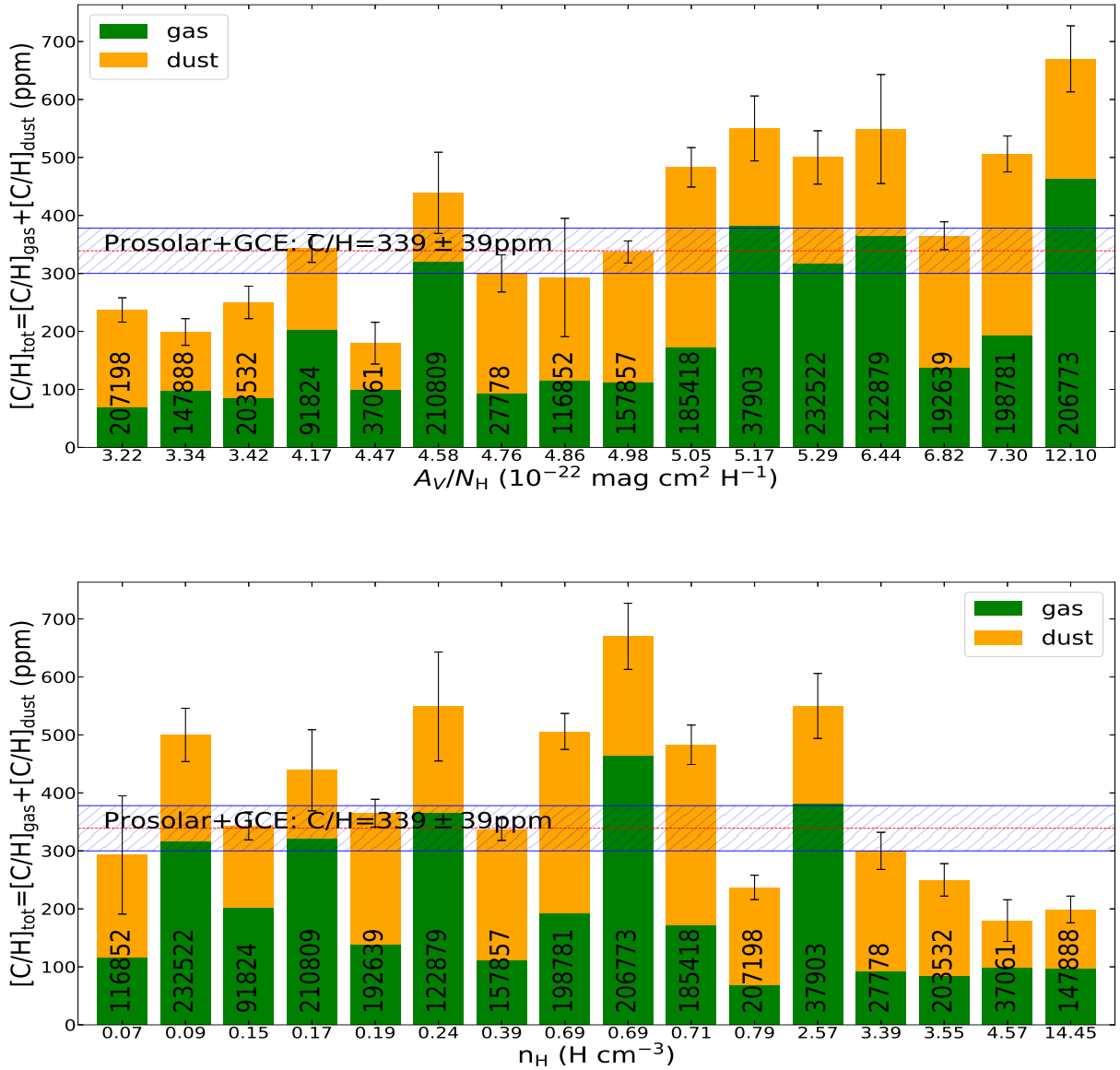


Fig. 22.— Comparison of the GCE-augmented protosolar C/H abundance ($[C/H]_{\text{ISM}} = 339 \pm 39$ ppm; blue horizontal shaded box) with $[C/H]_{\text{tot}}$ for each sight line, the gas-phase C/H abundance (green vertical boxes) plus the C/H depletion required by the dust extinction modeling to be locked up in graphitic dust (orange vertical boxes). The (vertical) error bars are for $[C/H]_{\text{tot}}$, resulting from the uncertainties in $[C/H]_{\text{gas}}$. The sources are ordered either in the extinction-to-gas ratio A_V/N_H (upper panel) or in the hydrogen number density (bottom panel).

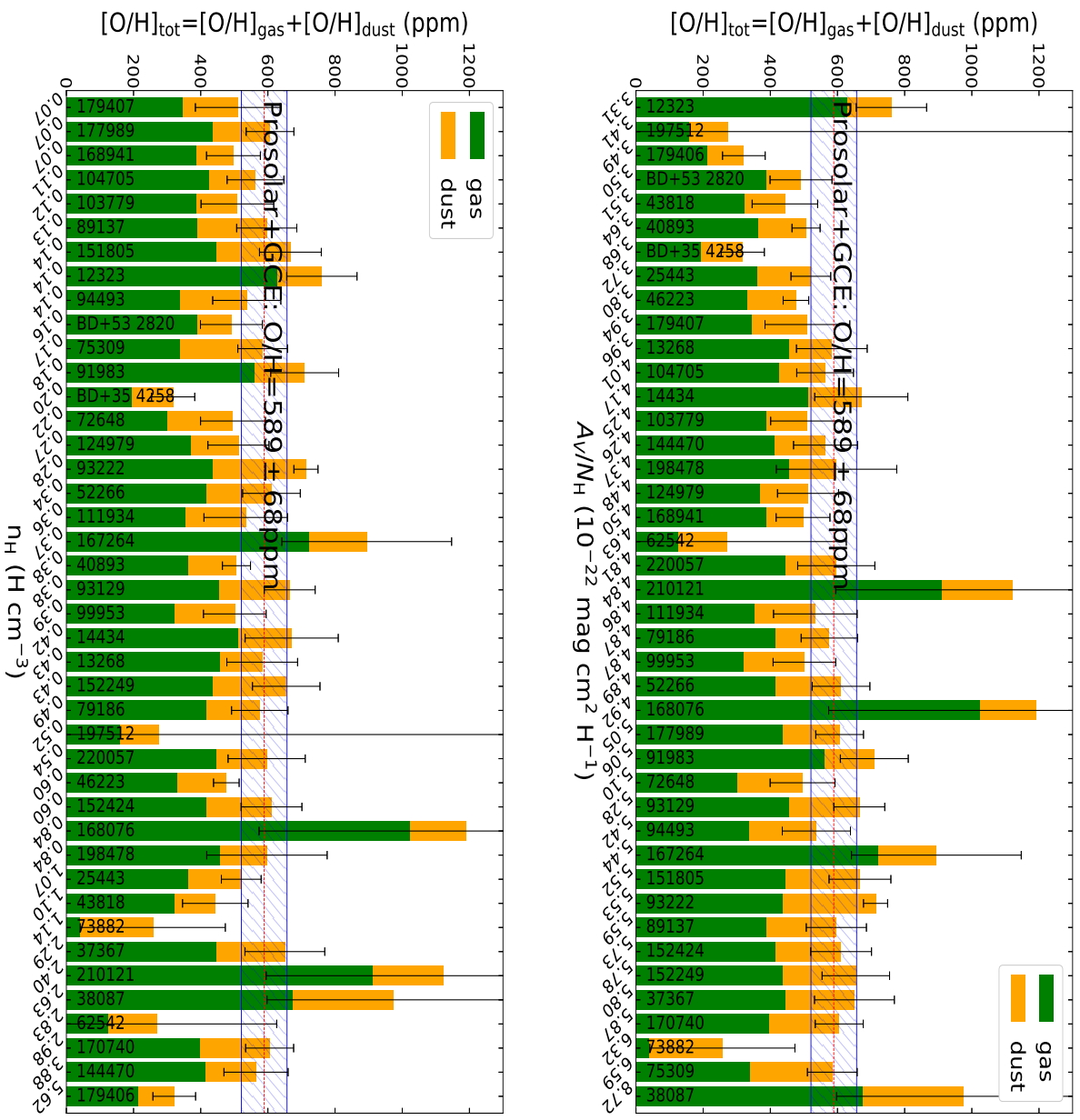


Fig. 23. — Same as Figure 22 but for oxygen.

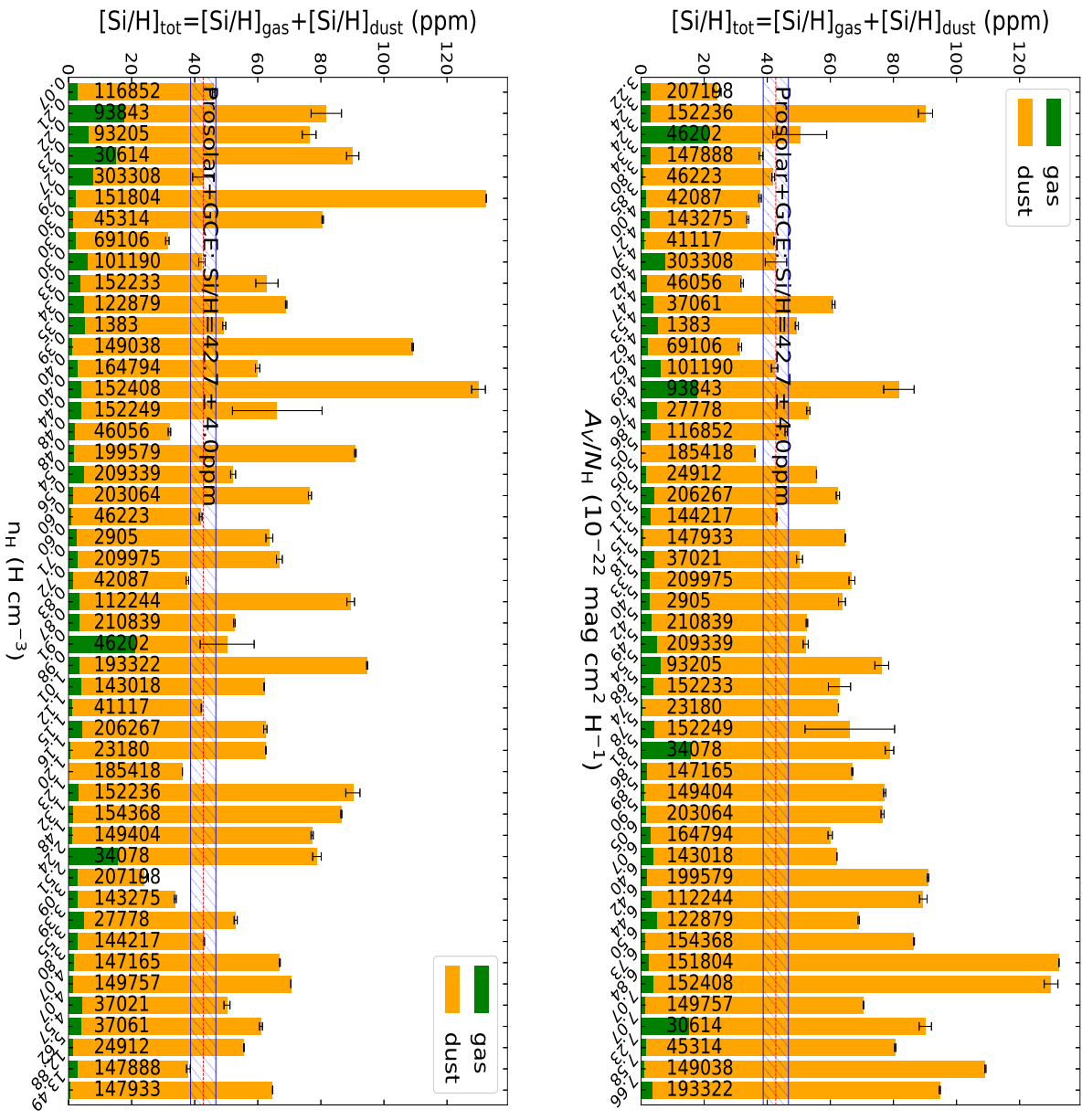


Fig. 24.— Same as Figure 22 but for silicon.

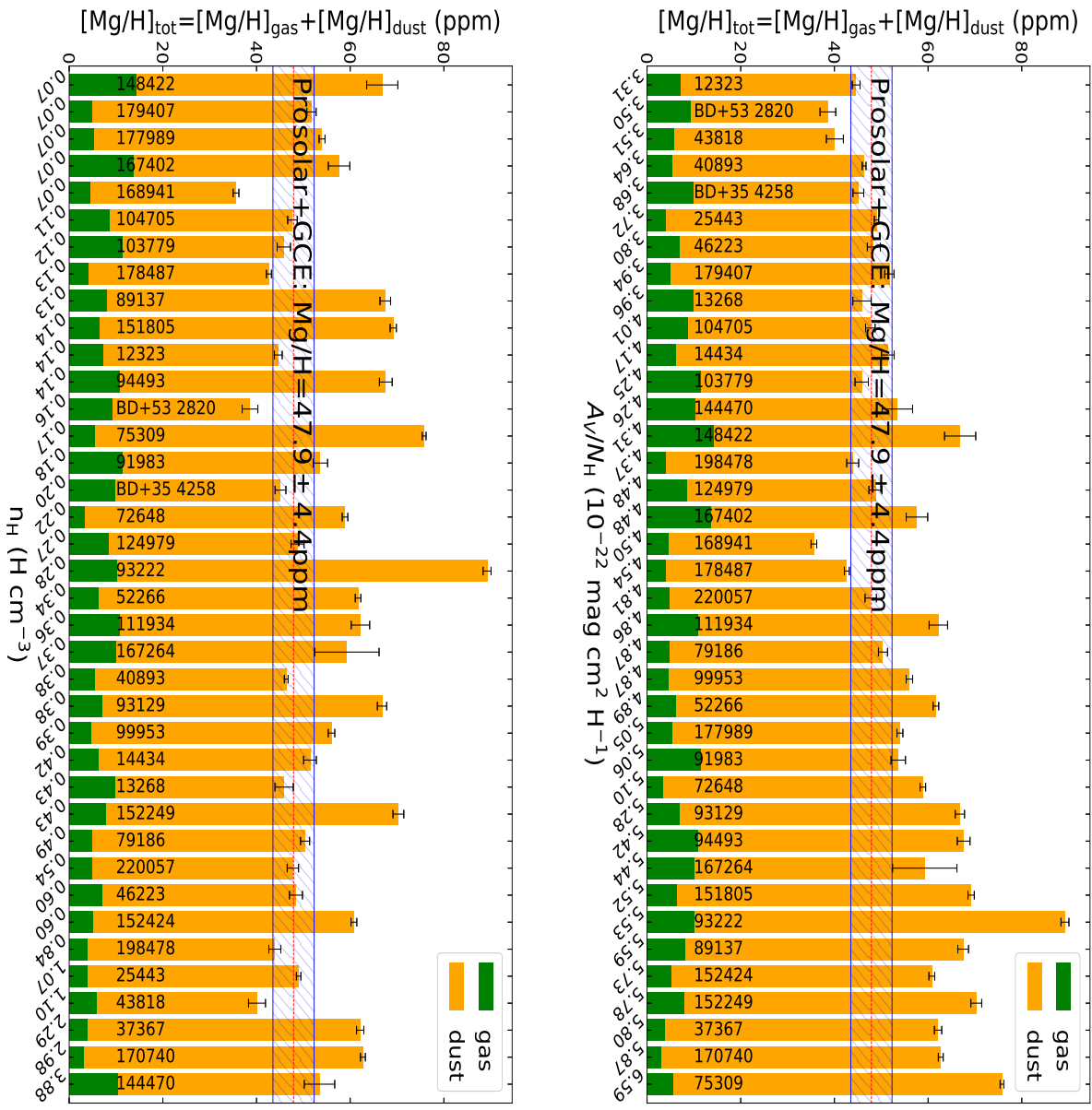


Fig. 25. — Same as Figure 22 but for magnesium.

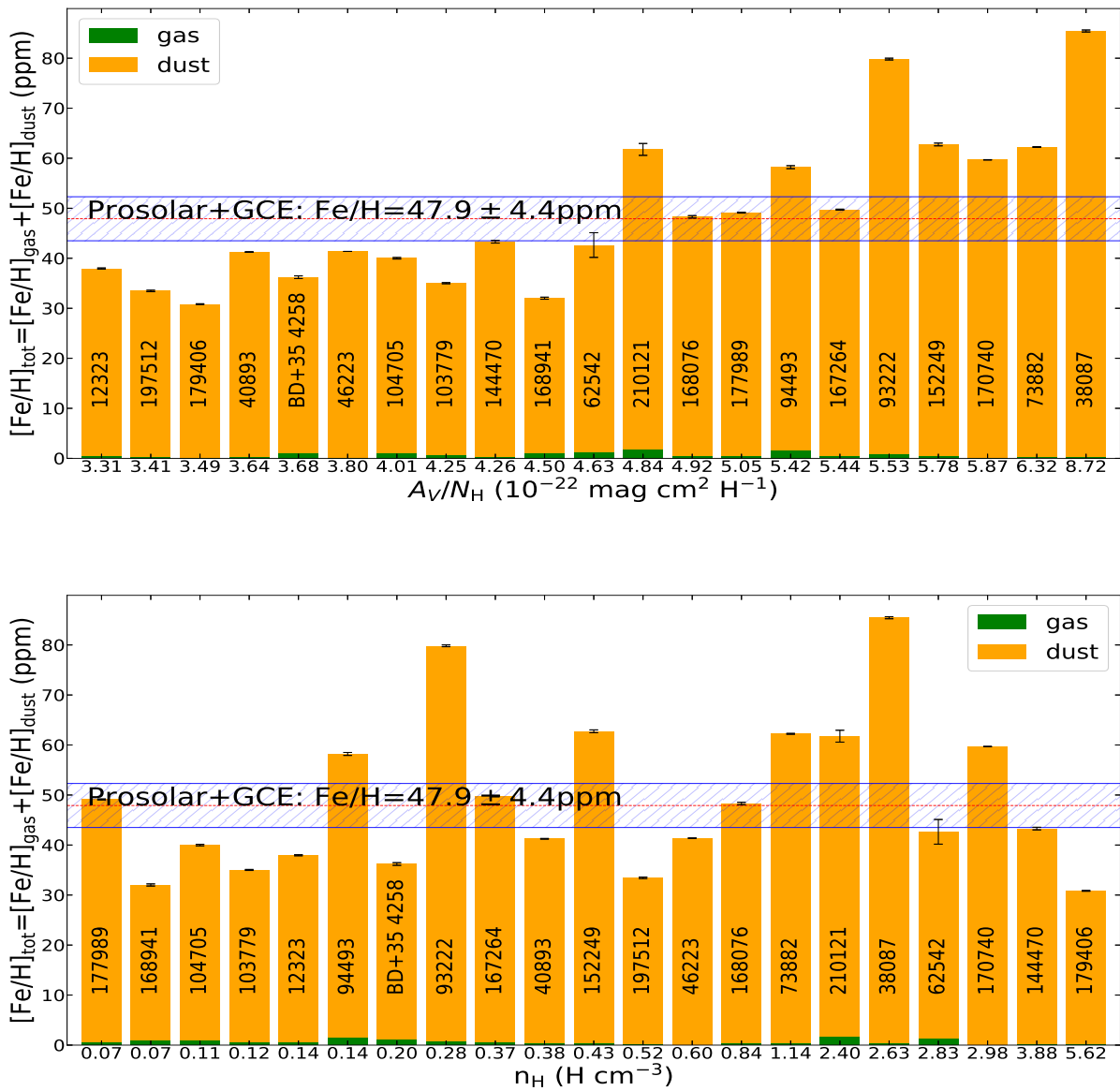


Fig. 26.— Same as Figure 22 but for iron.

Table 1. Extinction Parameters for the 81 Interstellar Sight Lines in Our Sample

Star	A_V^a (mag)	$E(B - V)^a$ (mag)	R_V^a	A_U^b (mag)	A_B^b (mag)	A_J^b (mag)	A_H^b (mag)	A_K^b (mag)	c_1^a	c_2^a	c_3^a	c_4^a	x_0^a (μm^{-1})	γ (μm^{-1})
BD+35 4258 ¹	0.67±0.24	0.25±0.04	2.68±0.53	1.06	0.90	0.20	0.08	0.08	1.334±0.474	0.139±0.039	0.421±0.124	0.088±0.035	4.618±0.017	0.651±0.222
BD+53 2820 ¹	0.88±0.15	0.29±0.03	3.04±0.32	1.36	1.18	0.26	0.08	0.10	1.372±0.621	0.156±0.026	0.682±0.107	0.255±0.063	4.591±0.015	0.732±0.041
HD 1383 ²	1.30±0.14	0.47±0.04	2.77±0.19	2.05	1.70	—	—	—	1.140±0.247	0.226±0.024	1.235±0.168	0.187±0.033	4.604±0.007	0.910±0.030
HD 12323 ¹	0.63±0.14	0.23±0.04	2.75±0.41	0.99	0.85	0.15	0.13	0.07	0.669±0.188	0.403±0.081	1.211±0.279	0.236±0.071	4.577±0.015	0.883±0.030
HD 13268 ²	1.09±0.15	0.36±0.04	3.02±0.24	1.71	1.45	—	—	—	0.959±0.740	0.284±0.039	0.735±0.143	0.313±0.061	4.577±0.011	0.756±0.025
HD 14434 ²	1.23±0.11	0.48±0.04	2.57±0.16	1.93	1.68	—	—	—	0.632±0.154	0.408±0.044	0.935±0.137	0.178±0.042	4.600±0.017	0.862±0.030
HD 24912	1.00±0.21	0.35±0.04	2.86±0.51	—	—	—	—	—	1.187±0.728	0.270±0.054	0.942±0.219	0.050±0.024	4.541±0.016	0.846±0.028
HD 25443 ¹	1.35±0.13	0.54±0.04	2.51±0.16	2.18	1.86	0.24	0.17	0.06	0.481±0.293	0.383±0.068	2.234±0.524	0.153±0.023	4.584±0.013	1.081±0.081
HD 27778 ¹	0.91±0.14	0.35±0.04	2.59±0.24	1.58	1.25	0.19	0.11	0.07	1.421±0.252	0.232±0.038	0.878±0.180	0.386±0.062	4.603±0.012	0.974±0.032
HD 30614	0.87±0.16	0.29±0.04	3.01±0.33	—	—	—	—	—	1.099±0.288	0.200±0.032	0.748±0.146	0.127±0.030	4.570±0.011	0.900±0.030
HD 37021	2.80±0.17	0.48±0.02	5.84±0.26	—	—	—	—	—	1.063±1.047	0.020±0.008	0.235±0.043	0.007±0.007	4.584±0.047	1.081±0.036
HD 37061 ¹	2.40±0.21	0.56±0.04	4.29±0.21	3.33	2.93	0.72	0.45	0.30	1.544±0.145	0.000±0.100	0.310±0.042	0.050±0.012	4.574±0.014	0.901±0.029
HD 37367 ¹	1.49±0.24	0.42±0.04	3.55±0.44	2.33	1.94	0.42	0.28	0.16	1.424±0.304	0.153±0.024	0.989±0.172	0.134±0.025	4.598±0.005	0.865±0.023
HD 37903 ¹	1.31±0.18	0.35±0.04	3.74±0.31	1.88	1.64	0.38	0.29	0.14	1.540±0.332	0.082±0.015	0.652±0.121	0.183±0.035	4.616±0.007	0.923±0.028
HD 38087 ¹	1.48±0.24	0.30±0.04	4.93±0.44	1.92	1.74	0.60	0.35	0.21	1.632±0.254	0.007±0.002	0.615±0.114	0.110±0.024	4.572±0.007	0.870±0.029
HD 40893 ¹	1.32±0.15	0.47±0.04	2.81±0.19	2.14	1.81	0.35	0.23	0.14	1.155±0.331	0.275±0.027	0.820±0.105	0.134±0.024	4.600±0.006	0.821±0.024
HD 42087	1.17±0.22	0.37±0.04	3.16±0.45	—	—	—	—	—	1.078±0.683	0.260±0.040	1.409±0.205	0.299±0.048	4.609±0.003	1.070±0.020
HD 43818	1.80±0.16	0.52±0.04	3.46±0.19	—	—	—	—	—	0.892±0.149	0.256±0.021	0.924±0.088	0.109±0.012	4.575±0.004	0.849±0.015
HD 46056 ¹	1.30±0.15	0.49±0.04	2.66±0.21	2.06	1.75	0.35	0.23	0.13	0.759±0.240	0.330±0.039	1.194±0.185	0.205±0.034	4.581±0.010	0.911±0.028
HD 46202 ¹	1.43±0.17	0.48±0.04	2.98±0.23	2.19	1.89	0.36	0.22	0.13	0.833±0.261	0.281±0.032	1.075±0.162	0.170±0.027	4.580±0.006	0.911±0.029
HD 46223	1.48±0.14	0.54±0.04	2.73±0.15	—	—	—	—	—	0.751±0.138	0.331±0.029	1.102±0.125	0.222±0.030	4.607±0.008	0.939±0.025
HD 52266 ¹	0.91±0.16	0.29±0.04	3.14±0.37	1.36	1.19	0.22	0.10	0.09	0.748±0.203	0.310±0.049	0.973±0.193	0.008±0.007	4.598±0.015	0.944±0.031
HD 62542 ¹	0.99±0.14	0.35±0.06	2.82±0.24	1.73	1.35	0.21	0.13	0.08	0.517±0.185	0.470±0.071	1.044±0.280	0.470±0.074	4.543±0.029	1.304±0.044
HD 69106	0.61±0.15	0.20±0.04	3.05±0.44	—	—	—	—	—	1.267±0.650	0.095±0.029	0.612±0.188	0.132±0.053	4.588±0.023	0.957±0.032
HD 72648 ¹	1.31±0.17	0.38±0.04	3.44±0.27	1.96	1.68	0.33	0.22	0.11	1.480±0.429	0.102±0.017	1.136±0.174	0.176±0.035	4.585±0.009	0.970±0.031
HD 73882 ¹	2.46±0.17	0.69±0.04	3.56±0.13	3.69	3.17	0.61	0.34	0.26	1.163±0.199	0.192±0.013	0.576±0.061	0.167±0.014	4.599±0.006	1.037±0.032
HD 75309 ¹	1.02±0.18	0.29±0.04	3.53±0.40	1.54	1.32	0.28	0.19	0.12	0.997±0.100	0.216±0.034	0.935±0.198	0.100±0.032	4.598±0.014	0.926±0.031
HD 79186	1.28±0.26	0.40±0.04	3.21±0.56	—	—	—	—	—	1.132±0.663	0.259±0.060	1.174±0.302	0.259±0.075	4.569±0.016	0.998±0.034
HD 89137	0.72±0.13	0.27±0.04	2.68±0.28	—	—	—	—	—	1.531±0.617	0.279±0.081	0.780±0.255	0.175±0.072	4.636±0.027	0.841±0.028
HD 91824 ¹	0.80±0.28	0.24±0.07	3.35±0.62	1.18	1.06	0.15	0.10	0.09	1.554±0.724	0.180±0.054	0.750±0.229	0.228±0.084	4.622±0.021	0.871±0.029
HD 91983 ¹	0.84±0.15	0.29±0.04	2.89±0.34	1.23	1.10	—	—	—	1.123±0.480	0.207±0.035	1.090±0.233	0.203±0.055	4.612±0.015	0.978±0.033
HD 93129	1.75±0.39	0.48±0.10	3.65±0.42	—	—	—	—	—	1.865±0.300	0.237±0.035	0.810±0.139	0.156±0.029	4.606±0.009	0.990±0.031
HD 93205	1.23±0.16	0.38±0.04	3.25±0.24	—	—	—	—	—	0.933±0.505	0.254±0.031	0.744±0.157	0.171±0.058	4.614±0.043	0.959±0.033
HD 93222 ¹	1.71±0.33	0.36±0.06	4.76±0.48	2.23	2.05	0.55	0.31	0.20	1.199±0.514	0.123±0.018	0.316±0.048	0.099±0.026	4.580±0.013	0.734±0.043
HD 93843	1.05±0.20	0.27±0.05	3.89±0.41	—	—	—	—	—	1.369±0.504	0.149±0.035	0.446±0.115	0.175±0.058	4.572±0.026	0.780±0.027
HD 94493	0.82±0.18	0.23±0.04	3.57±0.45	—	—	—	—	—	1.043±0.705	0.121±0.031	0.429±0.131	0.105±0.034	4.595±0.017	0.835±0.028
HD 99953	1.77±0.27	0.48±0.06	3.69±0.30	—	—	—	—	—	1.139±0.402	0.169±0.022	0.964±0.148	0.148±0.034	4.615±0.014	1.005±0.033
HD 101190 ²	0.92±0.12	0.37±0.04	2.48±0.21	1.40	1.25	—	—	—	0.405±0.094	0.399±0.057	1.295±0.231	0.208±0.047	4.625±0.015	1.078±0.035
HD 103779 ²	0.69±0.15	0.21±0.04	3.29±0.43	0.95	0.90	—	—	—	1.473±0.408	0.153±0.052	1.029±0.312	0.233±0.069	4.540±0.016	0.886±0.030
HD 104705 ¹	0.65±0.24	0.23±0.07	2.81±0.57	0.91	0.80	0.18	0.10	0.07	1.037±2.074	0.217±0.050	1.155±0.316	0.166±0.067	4.569±0.017	0.943±0.031
HD 111934	1.25±0.18	0.51±0.06	2.45±0.20	—	—	—	—	—	1.263±0.346	0.178±0.031	0.829±0.154	0.141±0.029	4.593±0.005	0.817±0.021
HD 116852	0.51±0.12	0.21±0.04	2.42±0.37	—	—	—	—	—	0.518±0.249	0.376±0.103	0.633±0.173	0.010±0.015	4.548±0.041	0.782±0.069
HD 122879 ²	1.13±0.20	0.36±0.05	3.15±0.30	1.69	1.45	—	—	—	1.321±0.299	0.233±0.040	1.243±0.230	0.190±0.039	4.581±0.004	0.831±0.021
HD 124979 ²	1.05±0.10	0.38±0.03	2.75±0.19	1.81	1.43	—	—	—	1.308±0.368	0.211±0.038	0.930±0.194	0.355±0.071	4.579±0.017	0.824±0.027
HD 144470 ¹	0.74±0.09	0.22±0.02	3.37±0.29	1.08	0.94	0.25	—	0.09	1.418±0.554	0.099±0.021	0.867±0.185	0.111±0.043	4.555±0.011	0.808±0.028
HD 147165 ¹	1.47±0.23	0.38±0.03	3.86±0.52	2.21	1.88	0.40	0.25	0.15	1.562±0.302	0.042±0.011	0.633±0.129	0.023±0.007	4.612±0.011	0.887±0.029
HD 147888 ¹	1.99±0.18	0.51±0.04	3.89±0.20	2.85	2.48	0.60	0.35	0.22	1.471±0.267	0.037±0.012	0.665±0.100	0.087±0.022	4.587±0.013	0.879±0.029
HD 148422 ²	0.88±0.16	0.29±0.04	3.02±0.33	1.35	1.17	—	—	—	0.401±0.114	0.391±0.070	0.644±0.143	0.192±0.048	4.601±0.014	0.776±0.025
HD 149757 ¹	0.82±0.13	0.32±0.04	2.55±0.24	1.26	1.09	0.27	0.14	0.10	1.002±0.100	0.286±0.037	1.872±0.313	0.215±0.052	4.552±0.010	1.186±0.042
HD 151805 ²	1.42±0.21	0.43±0.05	3.29±0.30	2.28	1.84	—	—	—	1.193±0.453	0.178±0.023	0.602±0.081	0.114±0.028	4.614±0.011	0.807±0.041

Table 1—Continued

Star	A_V^a (mag)	$E(B - V)^a$ (mag)	R_V^a	A_U^b (mag)	A_B^b (mag)	A_J^b (mag)	A_H^b (mag)	A_K^b (mag)	$c_1^{\prime a}$	$c_2^{\prime a}$	$c_3^{\prime a}$	$c_4^{\prime a}$	x_0^a (μm^{-1})	γ^a (μm^{-1})
HD 152236	2.24±0.26	0.60±0.03	3.73±0.39	—	—	—	—	—	0.764±0.665	0.258±0.049	1.291±0.369	0.150±0.029	4.610±0.023	1.104±0.094
HD 152249 ²	1.63±0.40	0.46±0.10	3.54±0.45	2.49	2.09	—	—	—	1.205±0.435	0.185±0.029	0.841±0.152	0.113±0.031	4.588±0.010	0.913±0.030
HD 152424	2.23±0.17	0.68±0.04	3.28±0.15	—	—	—	—	—	1.478±0.268	0.133±0.020	0.785±0.117	0.148±0.027	4.587±0.011	0.865±0.028
HD 154368	2.53±0.20	0.76±0.05	3.33±0.15	—	—	—	—	—	1.091±0.099	0.217±0.014	1.046±0.095	0.218±0.021	4.578±0.003	0.998±0.023
HD 157857 ²	1.48±0.17	0.43±0.04	3.45±0.23	2.41	2.04	—	—	—	1.548±0.269	0.057±0.021	1.115±0.203	0.263±0.049	4.563±0.011	0.848±0.028
HD 167264	0.98±0.15	0.30±0.04	3.26±0.31	—	—	—	—	—	1.514±0.510	0.085±0.022	0.726±0.141	0.138±0.041	4.596±0.016	0.819±0.033
HD 167402 ²	0.71±0.17	0.21±0.04	3.38±0.49	1.08	0.93	—	—	—	1.169±0.907	0.228±0.043	0.554±0.114	0.189±0.065	4.596±0.018	0.774±0.044
HD 168076 ²	2.64±0.17	0.76±0.04	3.47±0.12	3.61	3.33	—	—	—	0.977±0.483	0.164±0.019	0.740±0.101	0.123±0.017	4.604±0.007	0.972±0.021
HD 168941 ²	0.80±0.16	0.24±0.04	3.35±0.41	1.21	1.04	—	—	—	1.438±0.712	0.113±0.020	0.708±0.128	0.164±0.058	4.535±0.012	0.758±0.040
HD 170740 ¹	1.51±0.46	0.50±0.13	3.01±0.49	2.43	2.03	0.43	0.29	0.17	1.144±0.225	0.253±0.045	0.966±0.193	0.208±0.039	4.595±0.005	0.942±0.025
HD 177989 ¹	0.65±0.15	0.23±0.04	2.83±0.45	1.02	0.88	0.22	0.14	0.08	0.811±0.378	0.301±0.068	1.078±0.304	0.181±0.058	4.565±0.016	0.949±0.031
HD 178487 ²	1.04±0.15	0.35±0.04	2.98±0.27	1.61	1.35	—	—	—	0.902±0.691	0.224±0.038	1.045±0.222	0.103±0.033	4.576±0.016	0.842±0.028
HD 179406 ¹	0.96±0.14	0.35±0.04	2.73±0.25	1.55	1.29	0.31	0.26	0.08	1.530±0.333	0.164±0.027	1.210±0.209	0.236±0.044	4.607±0.008	0.948±0.030
HD 179407 ²	0.75±0.14	0.28±0.04	2.68±0.33	1.23	1.03	—	—	—	0.568±0.157	0.369±0.066	1.336±0.279	0.202±0.054	4.581±0.016	0.970±0.035
HD 185418 ¹	1.27±0.14	0.50±0.04	2.54±0.20	2.07	1.78	0.21	0.11	0.07	1.817±0.265	0.100±0.018	1.156±0.170	0.158±0.029	4.604±0.005	0.819±0.024
HD 192639 ²	1.91±0.16	0.61±0.04	3.14±0.16	2.98	2.50	—	—	—	1.248±0.238	0.190±0.020	1.008±0.130	0.148±0.027	4.575±0.010	0.866±0.029
HD 197512 ¹	0.94±0.30	0.33±0.09	2.84±0.50	1.62	1.33	0.16	0.06	0.08	0.773±0.248	0.339±0.067	1.593±0.345	0.180±0.046	4.573±0.006	1.029±0.028
HD 198478	1.48±0.17	0.57±0.04	2.60±0.19	—	—	—	—	—	1.257±0.419	0.259±0.027	1.456±0.182	0.251±0.039	4.567±0.011	1.014±0.032
HD 198781 ¹	0.75±0.13	0.35±0.04	2.14±0.28	1.22	1.04	0.10	0.07	0.06	0.663±0.381	0.474±0.090	1.912±0.506	0.271±0.054	4.590±0.013	1.125±0.067
HD 199579 ¹	1.14±0.28	0.36±0.04	3.17±0.69	1.82	1.51	0.27	0.14	0.11	1.099±0.552	0.279±0.065	0.807±0.211	0.202±0.059	4.593±0.013	0.986±0.033
HD 203532 ¹	0.94±0.11	0.28±0.03	3.37±0.24	1.56	1.26	0.27	0.12	0.08	0.758±0.165	0.267±0.034	1.502±0.246	0.204±0.036	4.599±0.011	1.266±0.040
HD 206267 ²	1.47±0.14	0.52±0.04	2.82±0.16	2.38	2.01	—	—	—	1.170±0.362	0.274±0.025	1.021±0.134	0.224±0.036	4.590±0.011	0.906±0.028
HD 206773 ²	1.99±0.21	0.45±0.04	4.42±0.26	2.72	2.50	—	—	—	1.018±0.283	0.154±0.014	0.504±0.078	0.049±0.015	4.583±0.016	0.893±0.030
HD 207198 ²	1.50±0.29	0.54±0.08	2.77±0.35	2.43	1.96	—	—	—	0.811±0.259	0.344±0.050	0.976±0.169	0.277±0.045	4.596±0.006	0.883±0.024
HD 209339 ¹	1.00±0.20	0.36±0.07	2.78±0.34	1.52	1.32	—	—	—	1.156±0.304	0.238±0.039	0.989±0.191	0.080±0.021	4.603±0.007	0.875±0.027
HD 210121 ¹	0.75±0.15	0.31±0.05	2.42±0.29	—	1.12	0.15	0.07	0.06	0.061±0.025	0.716±0.142	0.940±0.339	0.520±0.107	4.516±0.031	0.929±0.033
HD 210809	1.05±0.17	0.31±0.04	3.39±0.32	—	—	—	—	—	0.971±0.456	0.273±0.039	0.710±0.149	0.181±0.050	4.568±0.019	0.844±0.030
HD 210839	1.15±0.18	0.57±0.04	2.02±0.26	—	—	—	—	—	0.663±0.389	0.454±0.079	1.552±0.372	0.175±0.046	4.599±0.019	0.964±0.059
HD 220057 ¹	0.62±0.20	0.23±0.06	2.71±0.49	1.06	0.89	0.08	0.05	0.07	1.090±1.933	0.215±0.041	1.214±0.246	0.222±0.080	4.617±0.018	0.938±0.071
HD 232522	0.82±0.16	0.27±0.04	3.05±0.41	—	—	—	—	—	0.594±0.123	0.378±0.067	1.063±0.223	0.229±0.058	4.555±0.009	0.934±0.031
HD 303308	1.36±0.17	0.45±0.05	3.02±0.21	—	—	—	—	—	0.865±0.213	0.263±0.027	0.905±0.132	0.155±0.027	4.588±0.008	0.945±0.030

^a Data taken from Valencic et al. (2004).^b U, B, J, H and K extinction data taken from Fitzpatrick & Massa (2007) for those sight lines marked by “1” and from Gordon et al. (2009) for those marked by “2”.

Table 2. Hydrogen Densities and Gas-Phase C, O, Mg, Si and Fe Abundances of the 81 Interstellar Sight Lines in Our Sample

Star	N_{H} (10^{21} cm^{-2})	$f(\text{H}_2)$	$N(\text{HI})$ (10^{21} cm^{-2})	$N(\text{H}_2)$ (10^{21} cm^{-2})	$[\text{C}/\text{H}]_{\text{gas}}$ (ppm)	$[\text{O}/\text{H}]_{\text{gas}}$ (ppm)	$[\text{Mg}/\text{H}]_{\text{gas}}$ (ppm)	$[\text{Si}/\text{H}]_{\text{gas}}$ (ppm)	$[\text{Fe}/\text{H}]_{\text{gas}}$ (ppm)
BD+35 4258	$1.82^{+0.13}_{-0.29}$ (1)	0.04	$1.74^{+0.12}_{-0.28}$ (1)	0.04 ± 0.01 (1)	–	195.1 ± 64.3 (1)	10.00 ± 1.15 (1)	–	1.10 ± 0.26 (6)
BD+53 2820	$2.51^{+0.29}_{-0.35}$ (1)	0.1	$2.24^{+0.26}_{-0.36}$ (1)	$0.13^{+0.03}_{-0.04}$ (1)	–	389.0 ± 92.2 (1)	9.32 ± 1.68 (1)	–	–
HD 1383	$3.47^{+0.32}_{-0.40}$ (1)	0.18	$2.88^{+0.33}_{-0.40}$ (1)	3.09 ± 0.05 (1)	–	407.2 ± 71.2 (3)	7.59 ± 0.78 (1)	4.07 ± 374.92 (4)	0.15 ± 49.03 (4)
HD 12323	1.91 ± 0.18 (1)	0.19	$1.55^{+0.14}_{-0.18}$ (1)	$0.18^{+0.03}_{-0.05}$ (1)	–	629.8 ± 104.7 (1)	7.24 ± 0.83 (1)	–	0.55 ± 0.11 (6)
HD 13268	2.75 ± 0.38 (1)	0.21	2.19 ± 0.35 (1)	0.29 ± 0.05 (1)	–	457.5 ± 105.3 (1)	9.99 ± 1.95 (1)	–	–
HD 14434	2.95 ± 0.52 (23)	0.2	2.34 ± 0.54 (3)	0.30 ± 0.05 (3)	–	513.0 ± 138.6 (3)	6.31 ± 1.36 (23)	–	–
HD 24912	1.98 ± 0.54 (2)	0.34	1.20 ± 0.18 (3)	0.34 ± 0.07 (3)	163.1 ± 86.6 (34)	326.1 ± 97.5 (3)	1.99 ± 0.73 (2)	1.61 ± 0.44 (2)	0.92 ± 0.25 (13)
HD 25443	3.63 ± 0.42 (1)	0.46	$1.95^{+0.27}_{-0.23}$ (1)	0.83 ± 0.15 (1)	–	363.6 ± 59.2 (1)	4.08 ± 0.48 (1)	–	–
HD 27778	2.51 ± 0.44 (7)	0.49	0.89(5)	0.62(10)	79.2 ± 27.6 (14)	269.1 ± 53.8 (3)	1.05 ± 0.22 (7)	3.43 ± 0.60 (9)	0.10 ± 0.02 (9)
HD 30614	1.23 ± 0.28 (25)	0.36	0.93 ± 0.21 (27)	0.22 ± 0.09 (13)	–	723.6 ± 236.0 (24)	18.63 ± 7.74 (13)	12.59 ± 16.26 (4)	0.66 ± 0.40 (4)
HD 37021	4.79 ± 1.50 (7)	–	4.79 ± 1.50 (3)	–	90.9 ± 37.9 (14)	257.0 ± 82.6 (3)	1.78 ± 0.57 (7)	2.99 ± 1.15 (9)	0.58 ± 0.19 (9)
HD 37061	5.37 ± 1.20 (7)	–	5.37 ± 1.20 (3)	–	98.1 ± 35.5 (14)	316.2 ± 72.2 (3)	1.12 ± 0.26 (7)	0.19 ± 0.17 (4)	0.06 ± 0.08 (4)
HD 37367	2.57 ± 0.45 (23)	0.32	1.91 ± 0.44 (3)	0.41 ± 0.09 (29)	–	446.7 ± 118.9 (3)	3.89 ± 0.78 (23)	–	–
HD 37903	3.16 ± 0.47 (6)	0.53	1.45 ± 0.33 (3)	0.83 ± 0.12 (17)	332.1 ± 49.4 (15)	239.9 ± 37.4 (3)	1.12 ± 0.26 (7)	–	0.17 ± 0.06 (6)
HD 38087	1.70 ± 0.81 (6)	0.51	0.81 ± 0.81 (6)	0.44 ± 0.08 (17)	–	676.1 ± 376.5 (19)	–	–	0.33 ± 0.20 (6)
HD 40893	$3.63^{+0.25}_{-0.42}$ (1)	0.21	$2.88^{+0.27}_{-0.40}$ (1)	0.39 ± 0.03 (1)	–	363.6 ± 41.8 (1)	5.51 ± 0.40 (1)	–	0.42 ± 0.07 (6)
HD 42087	3.09 ± 0.71 (6)	0.21	0.98 ± 0.22 (27)	0.33 ± 0.11 (17)	–	1096.4 ± 605.1 (19)	–	1.41 ± 3.25 (4)	0.14 ± 0.13 (4)
HD 43818	5.13 ± 1.50 (23)	–	3.98 ± 1.30 (3)	–	–	323.7 ± 97.5 (3)	5.89 ± 1.81 (23)	–	–
HD 46056	3.39 ± 0.98 (19)	0.28	1.38 ± 0.48 (27)	0.48 ± 0.07 (17)	–	467.8 ± 181.5 (19)	–	1.66 ± 32.47 (4)	0.32 ± 0.12 (6)
HD 46202	4.79 ± 1.70 (19)	0.2	0.692 ± 0.18 (27)	0.48 ± 0.08 (17)	–	363.1 ± 206.2 (19)	–	17.78 ± 71.32 (4)	0.22 ± 9.82 (4)
HD 46223	$3.89^{+0.27}_{-0.18}$ (1)	0.24	$2.88^{+0.27}_{-0.13}$ (1)	$0.47^{+0.07}_{-0.05}$ (1)	–	331.6 ± 38.1 (1)	7.07 ± 1.39 (1)	0.89 ± 0.44 (4)	0.03 ± 0.00 (4)
HD 52266	$1.86^{+0.17}_{-0.21}$ (1)	0.11	$1.66^{+0.15}_{-0.19}$ (1)	0.10 ± 0.02 (1)	–	416.7 ± 85.9 (1)	6.28 ± 0.60 (1)	–	–
HD 62542	2.14 ± 1.00 (19)	0.6	0.79 ± 0.05 (5)	0.65 ± 0.40 (16)	–	125.9 ± 355.7 (19)	–	–	1.32 ± 2.46 (28)
HD 69106	1.29 ± 0.12 (1)	0.09	1.17 ± 0.11 (1)	0.06 ± 0.01 (1)	–	315.9 ± 46.6 (1)	6.02 ± 0.62 (1)	1.99 ± 0.49 (4)	0.40 ± 0.27 (4)
HD 72648	2.57 ± 0.41 (1)	0.39	$1.55^{+0.25}_{-0.21}$ (1)	0.50 ± 0.17 (1)	–	301.9 ± 96.6 (1)	3.39 ± 0.59 (1)	–	–
HD 73882	3.89 ± 0.68 (19)	0.66	1.29(57)	1.29 ± 0.26 (33)	–	430.7 ± 216.0 (19)	–	–	0.36 ± 0.08 (6)
HD 75309	$1.55^{+0.11}_{-0.18}$ (1)	0.19	$1.26^{+0.09}_{-0.17}$ (1)	$0.15^{+0.02}_{-0.03}$ (1)	–	339.0 ± 74.0 (1)	5.62 ± 0.41 (1)	–	–
HD 79186	2.63 ± 0.46 (23)	0.4	1.59 ± 0.36 (3)	0.53 ± 0.12 (3)	–	416.7 ± 84.0 (3)	4.90 ± 0.97 (23)	–	–
HD 89137	$1.29^{+0.18}_{-0.06}$ (1)	0.16	$1.07^{+0.17}_{-0.05}$ (1)	0.11 ± 0.02 (1)	–	388.9 ± 89.6 (1)	8.15 ± 1.14 (1)	–	–
HD 91824	1.45 ± 0.13 (1)	0.09	1.32 ± 0.12 (1)	$0.07^{+0.01}_{-0.02}$ (1)	145.3 ± 14.0 (15)	691.8 ± 104.6 (3)	10.93 ± 1.13 (1)	–	–
HD 91983	$1.66^{+0.19}_{-0.15}$ (1)	0.15	$1.41^{+0.20}_{-0.16}$ (1)	0.13 ± 0.02 (1)	–	562.2 ± 101.1 (1)	11.51 ± 1.54 (1)	–	–
HD 93129	$3.31^{+0.46}_{-0.31}$ (1)	0.1	$2.95^{+0.48}_{-0.27}$ (1)	$0.16^{+0.03}_{-0.02}$ (1)	–	456.0 ± 75.8 (1)	7.07 ± 0.99 (1)	–	–
HD 93205	2.40 ± 0.28 (1)	0.04	2.29 ± 0.26 (1)	$0.05^{+0.02}_{-0.01}$ (1)	–	375.2 ± 49.9 (20)	10.46 ± 1.30 (1)	4.90 ± 1.80 (4)	0.55 ± 0.37 (4)
HD 93222	$3.09^{+0.21}_{-0.29}$ (1)	0.04	$2.95^{+0.20}_{-0.27}$ (1)	0.059 ± 0.01 (1)	–	436.9 ± 35.9 (20)	10.23 ± 0.85 (1)	–	0.83 ± 0.18 (6)
HD 93843	$2.09^{+0.24}_{-0.19}$ (1)	0.04	$2.00^{+0.23}_{-0.18}$ (1)	0.04 ± 0.001 (1)	–	407.3 ± 96.6 (1)	8.52 ± 1.00 (1)	15.85 ± 430.77 (4)	0.93 ± 76.58 (4)
HD 94493	$1.51^{+0.174}_{-0.139}$ (1)	0.16	$1.26^{+0.17}_{-0.15}$ (1)	$0.12^{+0.02}_{-0.03}$ (1)	–	338.9 ± 101.4 (1)	10.97 ± 1.36 (1)	–	1.59 ± 0.30 (6)
HD 99953	3.63 ± 0.502 (1)	0.22	2.82 ± 0.45 (1)	0.40 ± 0.13 (1)	–	322.2 ± 93.3 (1)	4.79 ± 0.70 (1)	–	–
HD 101190	$2.24^{+0.16}_{-0.26}$ (1)	0.24	$1.77^{+0.12}_{-0.25}$ (1)	$0.27^{+0.03}_{-0.05}$ (1)	–	446.7 ± 69.0 (1)	8.71 ± 1.00 (1)	4.57 ± 71.47 (4)	0.54 ± 36.63 (4)
HD 103779	1.62 ± 0.19 (1)	0.1	1.48 ± 0.17 (1)	0.08 ± 0.02 (1)	–	389.1 ± 108.2 (1)	11.47 ± 1.42 (1)	–	0.66 ± 0.11 (6)
HD 104705	$1.62^{+0.19}_{-0.15}$ (1)	0.13	$1.41^{+0.20}_{-0.16}$ (1)	0.11 ± 0.02 (1)	–	426.7 ± 84.5 (1)	8.69 ± 1.02 (1)	–	1.02 ± 0.15 (6)
HD 111934	$2.57^{+0.36}_{-0.65}$ (1)	0.18	$2.09^{+0.29}_{-0.67}$ (1)	0.23 ± 0.08 (1)	–	354.8 ± 124.4 (1)	10.97 ± 1.97 (1)	–	–
HD 116852	1.02 ± 0.09 (1)	0.11	0.91 ± 0.08 (1)	0.06 ± 0.01 (1)	117.3 ± 103.2 (15)	537.5 ± 133.2 (1)	7.76 ± 0.74 (1)	2.57 ± 0.39 (4)	0.98 ± 0.35 (4)
HD 122879	$2.45^{+0.28}_{-0.23}$ (1)	0.17	$2.04^{+0.28}_{-0.24}$ (1)	$0.21^{+0.04}_{-0.03}$ (1)	324.3 ± 38.2 (15)	448.1 ± 72.8 (1)	6.44 ± 0.76 (1)	4.97 ± 0.61 (2)	0.53 ± 0.10 (6)
HD 124979	2.34 ± 0.38 (1)	0.21	1.86 ± 0.39 (1)	$0.25^{+0.03}_{-0.05}$ (1)	–	371.6 ± 90.9 (1)	8.53 ± 1.39 (1)	–	–
HD 144470	1.74 ± 0.300 (22)	0.13	1.51 ± 0.31 (22)	0.11 ± 0.02 (22)	–	414.3 ± 95.5 (24)	10.47 ± 3.25 (13)	–	0.32 ± 0.26 (13)
HD 147165	2.51 ± 0.510 (21)	0.05	2.40 ± 0.48 (21)	0.06 ± 0.01 (21)	–	371.5 ± 121.7 (21)	3.54 ± 0.73 (2)	1.96 ± 0.41 (2)	0.36 ± 24.68 (4)
HD 147888	$5.37^{+0.87}_{-2.10}$ (1)	0.11	$4.79^{+0.88}_{-2.10}$ (1)	$0.28^{+0.03}_{-0.05}$ (1)	105.4 ± 22.6 (14)	301.7 ± 50.6 (1)	1.86 ± 0.33 (1)	2.44 ± 0.60 (9)	0.15 ± 0.08 (6)
HD 148422	$2.04^{+0.38}_{-0.24}$ (1)	0.14	$1.74^{+0.36}_{-0.24}$ (1)	$0.14^{+0.04}_{-0.03}$ (1)	–	–	14.45 ± 3.33 (1)	–	–
HD 149757	1.40 ± 0.03 (2)	0.64	0.51 ± 0.02 (3)	0.45 ± 0.06 (3)	100.9 ± 48.6 (11)	307.1 ± 29.1 (8)	1.86 ± 0.16 (2)	1.50 ± 0.04 (2)	0.32 ± 0.09 (4)
HD 151805	2.57 ± 0.24 (1)	0.17	2.14 ± 0.25 (1)	$0.22^{+0.04}_{-0.05}$ (1)	–	447.4 ± 92.0 (1)	6.46 ± 0.67 (1)	–	–

2021.11.9.200: DRAFT

Table 2—Continued

Star	N_{H} (10^{21} cm^{-2})	$f(\text{H}_2)$	$N(\text{HI})$ (10^{21} cm^{-2})	$N(\text{H}_2)$ (10^{21} cm^{-2})	$[\text{C}/\text{H}]_{\text{gas}}$ (ppm)	$[\text{O}/\text{H}]_{\text{gas}}$ (ppm)	$[\text{Mg}/\text{H}]_{\text{gas}}$ (ppm)	$[\text{Si}/\text{H}]_{\text{gas}}$ (ppm)	$[\text{Fe}/\text{H}]_{\text{gas}}$ (ppm)
HD 152236	6.92±2.00(6)	0.16	5.89(79)	0.54±0.17(17)	—	2291.1±1034.8(19)	—	2.63±187.92(4)	0.18±0.07(6)
HD 152249	2.82±0.39(1)	0.14	2.40±0.39(1)	0.19±0.04(1)	—	436.4±100.5(1)	7.95±1.16(1)	4.17±14.20(4)	0.41±0.28(4)
HD 152424	3.89 ^{+0.45} _{-0.54} (1)	0.24	3.02 ^{+0.42} _{-0.49} (1)	0.47 ^{+0.05} _{-0.12} (1)	—	416.4±90.5(1)	5.24±0.62(1)	—	—
HD 154368	3.89±0.47(18)	0.75	1.00±0.11(16)	1.45±0.25(16)	—	338.7±179.5(19)	2.67±0.43(2)	1.49±0.24(2)	0.38±0.16(28)
HD 157857	2.75±0.48(23)	0.36	1.82±0.42(3)	0.49(29)	109.3±19.1(15)	467.7±92.4(3)	5.63±1.29(23)	—	—
HD 167264	1.80±0.30(24)	0.21	1.41±0.49(27)	0.19(26)	—	722.2±252.7(24)	10.11±6.88(13)	—	0.56±0.09(13)
HD 167402	1.58±0.15(1)	0.19	1.35 ^{+0.16} _{-0.12} (1)	0.15 ^{+0.03} _{-0.02} (1)	—	—	13.82±2.29(1)	—	—
HD 168076	5.37±3.10(18)	0.18	4.47±3.10(16)	0.48±0.10(16)	—	1023.3±617.2(19)	—	—	0.38±0.24(28)
HD 168941	1.78 ^{+0.16} _{-0.25} (1)	0.14	1.51 ^{+0.17} _{-0.24} (1)	0.13±0.02(1)	—	389.1±80.1(1)	4.68±0.61(1)	—	1.07±0.21(6)
HD 170740	2.57 ^{+0.36} _{-0.59} (1)	0.56	1.23 ^{+0.17} _{-0.48} (1)	0.72 ^{+0.13} _{-0.20} (1)	—	396.8±71.5(1)	3.16±0.53(1)	—	0.14±0.04(28)
HD 177989	1.29±0.15(1)	0.22	0.98 ^{+0.11} _{-0.14} (1)	0.15±0.04(1)	—	436.3±71.0(1)	5.37±0.63(1)	—	0.50±0.09(6)
HD 178487	2.29 ^{+0.21} _{-0.42} (1)	0.28	1.66 ^{+0.15} _{-0.38} (1)	0.32±0.07(1)	—	—	4.07±0.53(1)	—	—
HD 179406	2.75±0.71(6)	0.39	1.70±0.70(32)	0.54±0.09(17)	—	213.8±63.5(19)	—	—	0.14±0.07(6)
HD 179407	1.91 ^{+0.22} _{-0.35} (1)	0.18	1.58 ^{+0.22} _{-0.36} (1)	0.17 ^{+0.35} _{-0.04} (1)	—	346.9±126.2(1)	5.01±0.99(1)	—	—
HD 185418	2.63 ^{+0.24} _{-0.18} (1)	0.4	1.55 ^{+0.18} _{-0.14} (1)	0.53 ^{+0.09} _{-0.07} (1)	167.7±22.8(15)	380.2±43.8(1)	4.07±0.42(1)	0.06±0.01(12)	0.32±0.09(12)
HD 192639	3.09±0.71(18)	0.35	1.95±0.45(3)	0.54±0.14(3)	125.2±29.4(15)	446.6±110.9(3)	5.13±1.23(7)	—	0.32±0.11(28)
HD 197512	2.75±0.79(18)	0.33	1.82±0.75(31)	0.46±0.06(16)	—	158.5±1888.7(19)	—	—	0.30±0.15(28)
HD 198478	3.39 ^{+1.01} _{-0.94} (1)	0.34	2.09 ^{+0.58} _{-0.63} (1)	0.58 ^{+0.44} _{-0.46} (1)	—	457.4±179.3(1)	3.98±1.28(1)	—	—
HD 198781	1.48±0.17(1)	0.41	0.85 ^{+0.14} _{-0.06} (1)	0.30 ^{+0.06} _{-0.07} (1)	135.9±19.8(15)	501.0±73.9(1)	3.72±0.44(1)	—	—
HD 199579	1.78±0.31(18)	0.38	1.10(79)	0.34±0.03(16)	—	46.8±22.4(19)	—	1.62±0.34(4)	0.30±0.08(28)
HD 203532	2.75±0.48(23)	0.32	1.86±0.43(3)	0.44±0.09(3)	82.4±28.3(15)	257.0±46.4(3)	1.38±0.25(23)	—	—
HD 206267	3.09 ^{+0.36} _{-0.29} (1)	0.46	1.66 ^{+0.23} _{-0.15} (1)	0.71 ^{+0.13} _{-0.11} (1)	—	407.7±54.7(1)	3.56±0.44(1)	4.08±0.68(2)	0.22±0.06(28)
HD 206773	1.74 ^{+0.20} _{-0.12} (1)	0.3	1.23 ^{+0.20} _{-0.09} (1)	0.26 ^{+0.04} _{-0.05} (1)	426.4±50.2(15)	446.5±59.9(1)	5.50±0.65(1)	—	—
HD 207198	3.16 ^{+0.36} _{-0.44} (1)	0.39	1.91 ^{+0.31} _{-0.40} (1)	0.62±0.07(1)	102.1±25.1(14)	445.9±59.9(1)	3.64±0.43(1)	2.19±1.07(9)	0.43±0.08(9)
HD 209339	1.86±0.17(1)	0.15	1.58±0.15(1)	0.14 ^{+0.02} _{-0.03} (1)	—	355.0±52.3(1)	6.93±0.80(1)	5.06±0.88(2)	0.48±0.06(6)
HD 210121	1.55±0.40(6)	0.93	0.43±0.18(29)	0.72(29)	—	911.6±526.8(19)	—	—	1.74±1.19(6)
HD 210809	2.24 ^{+0.31} _{-0.26} (1)	0.08	2.04 ^{+0.28} _{-0.24} (1)	0.09 ^{+0.03} _{-0.02} (1)	295.3±48.6(15)	339.0±78.0(1)	10.94±1.69(1)	—	—
HD 210839	3.02±0.28(1)	0.42	1.74±0.20(1)	0.63±0.07(1)	—	490.1±56.4(1)	3.64±0.35(1)	3.48±0.40(2)	0.32±0.06(28)
HD 220057	1.29 ^{+0.29} _{-0.45} (1)	0.29	0.89 ^{+0.29} _{-0.47} (1)	0.19 ^{+0.04} _{-0.03} (1)	—	446.3±114.9(1)	4.90±1.22(1)	—	—
HD 232522	1.62±0.15(1)	0.19	1.32 ^{+0.12} _{-0.15} (1)	0.15 ^{+0.03} _{-0.04} (1)	296.6±36.4(15)	647.4±202.2(1)	8.69±0.83(1)	—	—
HD 303308	2.88 ^{+0.20} _{-0.47} (1)	0.11	2.57 ^{+0.18} _{-0.47} (1)	0.16 ^{+0.02} _{-0.03} (1)	—	423.0±35.9(20)	8.50±0.71(1)	7.08±658.80(4)	1.00±0.14(6)

(1) Jenkins (2019); (2) Gnačićski & Krogulec (2006); (3) Cartledge et al. (2004); (4) van Steenberg & Shull (1988); (5) Welty & Crowther (2010); (6) Jensen & Snow (2007a); (7) Jensen & Snow (2007b); (8) Knauth et al. (2006); (9) Miller et al. (2007); (10) Sheffer et al. (2007); (11) Sofia et al. (1994); (12) Sonnentrucker et al. (2003); (13) Jenkins et al. (1986); (14) Sofia et al. (2011); (15) Parvathi et al. (2012); (16) Rachford et al. (2002); (17) Rachford et al. (2009); (18) Jensen et al. (2007); (19) Jensen et al. (2005); (20) André et al. (2003); (21) Cartledge et al. (2008); (22) Cartledge et al. (2003); (23) Cartledge et al. (2006); (24) Meyer et al. (1998); (25) Crinklaw et al. (1994); (26) Federman et al. (1994); (27) Diplas & Savage (1994); (28) Snow et al. (2002); (29) Sheffer et al. (2008); (30) Welty & Crowther (2010); (31) Fitzpatrick & Massa (1990); (32) Hanson et al. (1992); (33) Cui et al. (2005); (34) Sofia et al. (2004).

Table 3. Model Parameters for Fitting the UV/Optical/Near-IR Extinction with a Mixture of Silicate and Graphite Grains

Star	A_V/N_H (10^{-22} mag cm 2 H $^{-1}$)	α_S	$a_{c,S}$ (μ m)	α_C	$a_{c,C}$ (μ m)	χ^2	[C/H] $_{\text{dust}}$ (ppm)	[Si/H] $_{\text{dust}}$ (ppm)
BD+35 4258	3.68	2.4	0.11	3.7	0.25	0.002	136	35
BD+53 2820	3.5	2.9	0.17	3.7	0.28	0.003	151	29
HD 12323	3.31	3.15	0.18	3.9	0.34	0.001	134	37
HD 13268	3.96	3.4	0.29	3.55	0.19	0.002	185	36
HD 14434	4.17	3.1	0.14	3.65	0.22	0.001	181	45
HD 25443	3.72	3.24	0.22	4.02	0.14	0.001	154	45
HD 37367	5.8	2.4	0.14	3.89	0.4	0.002	175	58
HD 38087	8.72	1.26	0.1	3.63	0.54	0.001	244	85
HD 40893	3.64	2.8	0.15	3.85	0.38	0.001	123	41
HD 43818	3.51	2.88	0.18	3.75	0.29	0.002	127	34
HD 46223	3.8	3.1	0.17	3.75	0.25	0.001	154	41
HD 52266	4.89	2.82	0.16	3.88	0.44	0.001	159	55
HD 62542	4.63	3.54	0.12	2.18	0.06	0.001	237	41
HD 72648	5.1	2.25	0.14	3.88	0.24	0.001	135	56
HD 73882	6.32	2.8	0.16	2.92	0.15	0.001	213	62
HD 75309	6.59	2.7	0.17	3.83	0.35	0.002	201	70
HD 79186	4.87	3	0.18	3.52	0.25	0.001	202	45
HD 89137	5.59	2.64	0.12	3.5	0.21	0.001	196	59
HD 91983	5.06	2.78	0.13	3.36	0.14	0.001	223	42
HD 93129	5.28	2.6	0.16	3.3	0.26	0.001	137	60
HD 93222	5.53	2.38	0.19	3.4	0.1	0.001	45	79
HD 94493	5.42	2.4	0.13	3.6	0.45	0.001	162	57
HD 99953	4.87	2.52	0.15	3.75	0.54	0.001	154	51
HD 103779	4.25	2.78	0.17	3.25	0.1	0.003	163	34
HD 104705	4.01	2.84	0.15	3.83	0.29	0.001	162	39
HD 111934	4.86	2.8	0.15	3.9	0.28	0.002	191	51
HD 124979	4.48	3.2	0.21	3.73	0.3	0.002	213	40
HD 144470	4.26	2.2	0.14	3.9	0.2	0.002	129	43
HD 148422	4.31	3.35	0.26	3.78	0.35	0.001	165	52
HD 151805	5.52	2.61	0.16	3.8	0.34	0.001	153	63
HD 152249	5.78	2.54	0.15	3.8	0.49	0.001	170	62
HD 152424	5.73	2.32	0.12	3.72	0.39	0.001	191	56
HD 167264	5.44	2.05	0.1	3.85	0.48	0.003	183	49
HD 167402	4.48	2.83	0.16	3.6	0.42	0.002	170	44
HD 168076	4.92	2.55	0.13	3.6	0.5	0.001	185	48
HD 168941	4.5	2.48	0.12	3.6	0.3	0.003	208	31
HD 170740	5.87	2.75	0.13	3.66	0.45	0.001	230	60
HD 177989	5.05	2.9	0.13	3.7	0.32	0.001	223	49
HD 178487	4.54	2.83	0.14	3.95	0.5	0.003	210	39
HD 179406	3.49	2.42	0.1	3.7	0.32	0.001	150	31
HD 179407	3.94	2.98	0.15	3.93	0.3	0.001	147	47
HD 197512	3.41	2.88	0.13	3.78	0.33	0.001	152	33
HD 198478	4.37	2.66	0.1	3.66	0.3	0.001	200	40
HD 210121	4.84	3.55	0.17	2.8	0.06	0.002	215	60
HD 220057	4.81	2.7	0.11	3.8	0.32	0.002	215	43